An accurate approach to simulate friction stir welding processes using adaptive formulation refinement

H. Venghaus [a],[*], M. Chiumenti [a], J. Baiges [b],[a], D. Juhre [c], I. Castañar [b]

[a] *International Center for Numerical Methods in Engineering (CIMNE), Polytechnic University of Catalonia (UPC), Campus Norte UPC, 08034 Barcelona, Spain*
[b] *Polytechnic University of Catalonia (UPC), Barcelona Tech, Jordi Girona 1-3, Edifici C1, 08034 Barcelona, Spain*
[c] *Institute of Mechanics (IFME), Otto von Guericke University Magdeburg (OVGU), Universitätsplatz 2, 39106 Magdeburg, Germany*

ARTICLE INFO

ABSTRACT

A novel *Adaptive Formulation Refinement* (AFR) strategy for Friction Stir Welding (FSW) problems is presented. In FSW, the accurate computation of strains is crucial to correctly predict the highly non-linear material behavior in the stir zone. Based on a posteriori error estimation, AFR switches between two mixed formulations depending on the required accuracy in the different regions of the domain. The higher accuracy formulation is used in the thermo-mechanically affected zone (TMAZ), while a computationally cheaper formulation is used elsewhere. AFR adds to the well-known h- (mesh size), p- (polynomial degree) and r-refinement (spatial distribution) approaches. The considered mixed formulations are the velocity/pressure ($\mathbf{u}/p$) and the velocity/pressure/deviatoric strain rate ($\mathbf{u}/p/\mathbf{e}$) formulations—both suitable for isochoric material flow. By applying the AFR strategy, the use of linear elements is preserved, the incompressible flow of the material is captured correctly and any remeshing is avoided. Furthermore, the treatment of the interface between refined and unrefined subdomains is straightforward due to the compatibility of variable fields and lack of hanging nodes. The accuracy of the results obtained from the AFR method compares favorably with reference results of the non-adaptive $\mathbf{u}/p/\mathbf{e}$ formulation. At the same time, faster build and solve times are achieved.

1. Introduction

Friction Stir Welding (FSW) is a solid-state joining process, where two facing work pieces are welded together using a non-consumable pin-tool which rotates and moves along their interface. In FSW, the joining process is achieved because of heat generated by friction between the pin-tool shoulder and the work pieces as well as by the plastic deformation of the stirred material. Typically, the material is not melted. This is a great advantage over conventional welding techniques, since both solidification and liquation cracking are avoided. However, the FSW process is very sensitive to the process parameters such as the rotation speed, the advancing speed, the pin shape and tilting, among others. The numerical simulation of FSW is a valuable tool to understand the influence of these parameters to optimize the process [1].

The main goals of the simulation of FSW are: the prediction of the temperature distribution [2,3], the sensitivity to the process parameters [4], the analysis of the strain rate field [5] and the material flow [6,7] as well as the contact and friction [8,9]. The choice of the most suitable computational frameworks (i.e., Eulerian, Lagrangian or ALE) has also been analyzed [10]. Furthermore,

* Corresponding author.
 E-mail address: hvenghaus@cimne.upc.edu (H. Venghaus).

several works are devoted to the evolution of the metallurgy in the Heat Affected Zone (HAZ) [11] and the formation of different defects induced by the welding process [6].

The material characterization in FSW simulations is also of great scientific interest because of the strong thermo-mechanical coupling. On one hand, the thermal analysis is driven by the heat generated by the plastic dissipation (material stirring and friction between tool and work piece). On the other hand, the thermal softening, induced by the temperature field, must be accounted for, in order to characterize both material stiffness and strength accurately. Moreover, the isochoric nature of the plastic deformations (i.e., J_2-plasticity or visco-plastic flow models) must be considered [12]. As a consequence, the use of standard (displacement-based) formulations is typically precluded and more sophisticated Finite Element technologies are mandatory in order to deal with the inherent material incompressibility.

Established methods to deal with isochoric behavior are the *Reduced and Selective Integration* method [13–15], *B-bar* and *F-bar* approaches [16–19], the *Enhanced Assumed Strain* methods [20–22] or the *Q1P0 Formulation* [23]. Unfortunately these methods are often only applicable to nearly incompressible cases and/or are not compatible with arbitrary types of elements and choices of shape functions. Another approach to deal with incompressible behavior is the use of Discontinuous Galerkin methods [24–26].

The mixed velocity/pressure ($\mathbf{u}/p$) formulation is an alternative approach to deal with a fully isochoric behavior, regardless of the element type (e.g., hexahedral, tedrahedral or prism elements are allowed) and thus facilitating the mesh generation when complex industrial tools are used. Stabilization techniques and, particularly, the Variational Multi-Scale (VMS) method [27,28] have been introduced to overcome the limitation on the compatibility among the interpolation degrees of the nodal variables. This approach, originally developed for incompressible computational fluid dynamics (CFD) analysis, has been extended to solid mechanics [29] to deal with elasto-plasticity, damage and strain localization problems [30–35], hyper-elasticity [36,37] and elasto-dynamics, including finite strain solid dynamics [38–41]. Throughout the present paper the $\mathbf{u}/p$ formulation will also be referred to as the *two-field* formulation.

To enhance the accuracy of the solution of a Finite Element simulation, the most frequently applied techniques are: the use of finer meshes (*h*-refinement), higher order shape functions (*p*-refinement) or a combination of both (*hp*-refinement [42,43]). Unfortunately, *p*-refinement is not straightforward for the $\mathbf{u}/p$ formulation. However, mixed formulations, considering either the stress or strain as an additional primary unknown, have proven to be a good alternative to the use of higher order shape functions.

The mixed (linear/linear) displacement/stress ($\mathbf{u}/\sigma$) formulation [44,45] was developed to enhance the solution accuracy by considering the stresses, additionally to the displacements, as primary unknowns. By splitting the stress tensor into its volumetric (i.e., the pressure p) and its deviatoric part ($\mathbf{s}$), it is possible to define a three-field $\mathbf{u}/p/\mathbf{s}$ formulation [46] able to combine the material incompressibility requirement with stress accuracy.

However, several material laws are strain driven. Therefore, the mixed displacement/strain ($\mathbf{u}/\varepsilon$) formulation [44,47,48] was proposed. Finally, the novel displacement/pressure/deviatoric strain ($\mathbf{u}/p/\mathbf{e}$) formulation [12] combines both the $\mathbf{u}/p$ and $\mathbf{u}/\varepsilon$ formulations. The $\mathbf{u}/p/\mathbf{e}$ formulation yields a faster convergence rate upon mesh refinement when compared to the classical $\mathbf{u}/p$ formulation and shows an enhanced accuracy for the same number of degrees of freedom. It has also proven to be a valuable tool in the analysis of non-linear, inelastic behavior [49] and topology optimization [50]. Throughout the present paper the $\mathbf{u}/p/\mathbf{e}$ formulation will also be referred to as the *three-field* formulation.

When simulating FSW processes however, the solution is smooth in most regions of the computational domain. Therefore the use of the very sophisticated and CPU-expensive $\mathbf{u}/p/\mathbf{e}$ formulation is unnecessary in most parts of the domain. Only close to the pin, where high temperature gradients and strain rates are observed, the $\mathbf{u}/p/\mathbf{e}$ formulation is required. In order to define the most suitable and computationally efficient framework for the FSW simulation, an adaptive use of both two- and three-field formulations is presented in this work. This Adaptive Formulation Refinement (AFR) approach is driven by an a posteriori error estimator [51–54]. Thus, it is possible to switch between the $\mathbf{u}/p$ and $\mathbf{u}/p/\mathbf{e}$ formulation according to the required solution accuracy, while preserving the use of linear elements and avoiding any remeshing. Furthermore, it can be shown that the treatment of the interface between unrefined ($\mathbf{u}/p$) and refined ($\mathbf{u}/p/\mathbf{e}$) subdomains is straightforward, due to the compatibility of the variable fields and the lack of hanging nodes.

The main novelty of the present paper is the element-wise use of differently accurate (and computationally demanding) mixed and stabilized FE formulations as a means of adaptive refinement strategy. The presented paper shows that the superior strain rate accuracy of the three-field formulation can be applied in crucial areas of the computational domain while the overall computational cost is reduced by using the two-field formulation elsewhere. A reasonable subdivision of the computational domain into $\mathbf{u}/p$ and $\mathbf{u}/p/\mathbf{e}$ elements is key to minimizing the global error with respect to the computational cost and is therefore discussed in detail in the present paper. The focus lies on the demonstration of the capabilities of this novel approach to adaptive refinement. Hence, the modeling of the FSW process is kept as simple as possible. To assess the results several numerical examples are presented.

The outline of the present paper is as follows: In Section 2 the governing equations for the mechanical problem are introduced and the visco-plastic material model is introduced in Section 2.2. Section 2.3 introduces the weak form and element stiffness matrices for the $\mathbf{u}/p$ formulation (Section 2.3.1) and the $\mathbf{u}/p/\mathbf{e}$ formulation (Section 2.3.2), respectively. In Section 3 the thermal problem is introduced. In Section 4 the AFR approach is introduced, including the error estimators (Section 4.1), the adaptive approach (Section 4.3) as well as the solution strategy (Section 4.4). The results are presented and assessed in Section 5 and conclusions are drawn in Section 6.
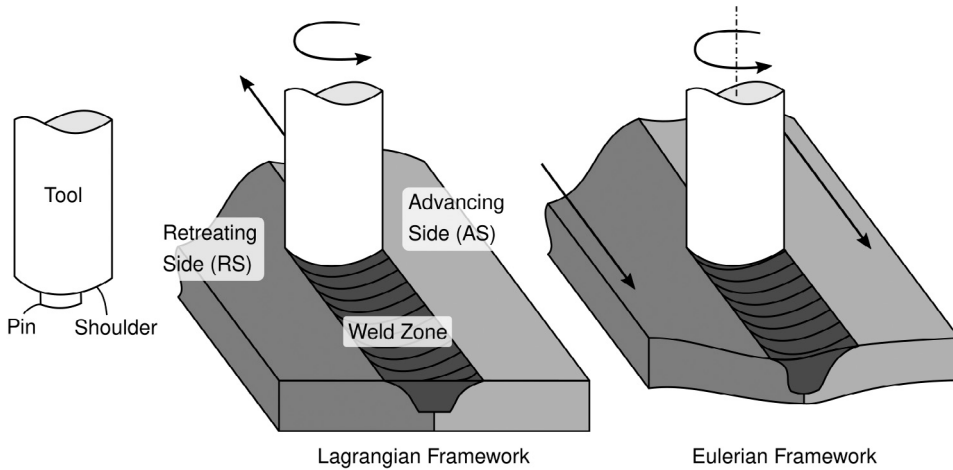
Fig. 1. Friction Stir Welding Process.

2. Mechanical analysis

In Friction Stir Welding a pin-tool is rotating around its axis while moving forward along the welding line. Thus, assuming a Lagrangian framework, it is necessary to perform continuous remeshing to adjust the mesh according to the current tool position. Alternatively, it is possible to consider a relative movement of the metal sheets towards the actual pin which is kept rotating around a fixed axis. In this case, the problem is solved in an Eulerian framework [29] (see Fig. 1).

The advantage of the Eulerian framework is the minimization of remeshing, particularly when a cylindrical tool is used. Bussetta et al. [10] showed that both frameworks yield equivalent results, though the Eulerian framework is generally preferred because it is computationally more efficient. The main consequence of adopting an Eulerian framework is related to the constitutive model used to characterize thermo-mechanical material behavior. The classical thermo-elasto-visco-plastic model, used within the Lagrangian framework, is typically replaced by a thermo-visco-plastic flow model, as introduced in Section 2.2.

2.1. Continuum problem

Let Ω denote the open and bounded domain in $\mathbb{R}^n$ occupied by the body defined in a space of n dimensions. The boundary Γ of Ω is split into Γ_u, where the prescribed velocities $\bar{\mathbf{u}}$ are specified (Dirichlet boundary conditions), and Γ_t, where the prescribed tractions $\bar{\mathbf{t}}$ are applied (Neumann boundary conditions), such that $\Gamma_u \cup \Gamma_t = \Gamma$ and $\Gamma_u \cap \Gamma_t = \emptyset$.

The mechanical model is described by the following set of equations

$$\nabla \cdot \mathbf{s} + \nabla p + \mathbf{b} = \mathbf{0} \tag{1}$$

$$\mathbf{e} - \nabla^s \mathbf{u} = \mathbf{0} \tag{2}$$

$$\mathbf{s} - 2\mu_{\text{eff}} \mathbf{e} = \mathbf{0} \tag{3}$$

$$\nabla \cdot \mathbf{u} = 0, \tag{4}$$

where Eq. (1) is the balance of momentum equation, Eq. (2) the kinematic equation, Eq. (3) the constitutive equation, and, finally, Eq. (4) enforces the incompressibility constraint. In the above equations, $\mathbf{u}$ denotes the velocity field, being the driving variable of the problem, p and $\mathbf{s}(\mathbf{e})$ are the spherical (pressure) and the deviatoric parts of the stress tensor, μ_{eff} is the effective viscosity and $\mathbf{b}$ are the body forces. The strain rate tensor, $\mathbf{e} = \nabla^s \mathbf{u}$, is purely deviatoric due to the isochoric nature of this problem (incompressible flow). Observe that the convective term of the balance of momentum equation is neglected because in FSW the material flow is characterized by very low Reynolds numbers (the viscous forces being much larger than the inertial forces [12,29]).

2.2. Norton–Hoff material model

Visco-plastic behavior is widely used to describe the material flow for the simulation of several metal forming processes such as metal casting, extrusion or forging. Such laws neglect the elastic response and assume an incompressible material flow. Common visco-plastic material models are the Sheppard–Wright model [55], the (regularized) Bingham model [56], the Carreau model [57] and the Norton–Hoff model [58,59], which is a generalization of a non-Newtonian fluid, modeled as a power law. In the present work, the Norton–Hoff model is used because of the availability of temperature-dependent material parameters (see Fig. 19), obtained from an extensive experimental program.
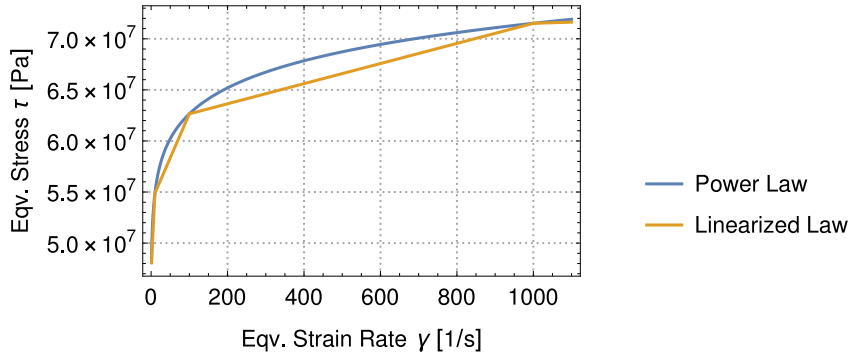
Fig. 2. Norton–Hoff power law and linearized law at a fixed temperature of $T = 300\,^\circ$ C.

The stresses **s** are obtained as

$$\mathbf{s} = 2\mu_{\text{eff}}\mathbf{e} \quad \text{with} \quad \mu_{\text{eff}}(\gamma) = \mu_0\gamma^{m-1}, \tag{5}$$

where the effective viscosity μ_{eff} is computed from the (temperature-dependent) consistency parameter μ_0, the equivalent strain rate $\gamma = \sqrt{2}\|\mathbf{e}\|$ and the (temperature-dependent) flow index m. Note that for $m = 1$ *Newtonian* behavior is recovered, thus $\mu_{\text{eff}} = \mu_0$. In the present work, the flow index m ranges from 0.02 to 0.2, resulting in very non-linear behavior and leading to a *shear-thinning* effect at the boundary layer.

The mechanical dissipation D_{m} is computed as

$$D_{\text{m}} = \varphi\,\mathbf{s} : \mathbf{e}, \tag{6}$$

where φ is the fraction of the mechanical dissipation turned into heat.

Analogous to the equivalent strain rate, an equivalent stress τ can be computed as $\tau = \frac{\sqrt{2}}{2}\|\mathbf{s}\|$. Thus, the constitutive equation can also be written as $\tau = \mu_{\text{eff}}\gamma$ and the mechanical dissipation reduces to $D_{\text{m}} = \varphi\tau\gamma$.

Linearized law. Due to the highly non-linear nature of the constitutive equation for very low values of the flow index parameter m, a linearized version of the Norton–Hoff law is proposed. For each order of magnitude of the equivalent strain rate γ, a modified effective viscosity $\bar{\mu}_{\text{eff}}$ is computed by interpolating the values obtained at the two extremes $\mu_{\text{eff}1}$ and $\mu_{\text{eff}2}$.

First, the order of magnitude of the equivalent strain rate is determined to the smaller whole number ψ as

$$\psi = \lfloor \log_{10}\gamma \rfloor \quad \text{for} \quad \gamma > 1. \tag{7}$$

Then, two equivalent strain rates are computed as $\gamma_1 = 10^{\psi}$ and $\gamma_2 = 10^{\psi+1}$ and, according to Eq. (5), two effective viscosities $\mu_{\text{eff}1}$ and $\mu_{\text{eff}2}$ are computed. Finally, by performing a linear interpolation, the value of the modified effective viscosity $\bar{\mu}_{\text{eff}}$ is obtained. For values of $\gamma \leq 1$, the linearized effective viscosity is computed as $\bar{\mu}_{\text{eff}} = \mu_{\text{eff}}(\gamma = 1)$.

Fig. 2 shows the equivalent stress/strain rate curves of both the original and the linearized Norton–Hoff model for a constant temperature T.

2.3. Mixed finite element formulations

Two of the main challenges of simulating FSW are the isochoric material flow and the highly non-linear material behavior induced by the thermal softening. In the present work, mixed formulations are used to address both challenges. The mixed velocity/pressure ($\mathbf{u}/p$) formulation is typically used in CFD analysis to deal with *fully* incompressible fluid flows. This formulation allows for the use of arbitrary element types such as hexahedral, tetrahedral or prism elements as well as arbitrary orders of shape functions. Nevertheless, linear–linear shape functions are generally used to interpolate both the velocity and pressure fields [44]. Alternatively, the mixed velocity/pressure/deviatoric strain rate ($\mathbf{u}/p/\mathbf{e}$) formulation can be adopted. This three-field formulation has shown a superior stress/strain rate accuracy while also dealing with fully incompressible behavior [12]. However, the $\mathbf{u}/p/\mathbf{e}$ formulation is also computationally more expensive because it introduces the deviatoric strain rate tensor as a primary unknown, together with the velocity and the pressure fields.

The main objective of the present work is to enhance the efficiency of FSW simulations by using the $\mathbf{u}/p/\mathbf{e}$ formulation only in the regions of the computational domain where the enhanced stress/strain rate accuracy is required, while using the $\mathbf{u}/p$ formulation elsewhere.

In the following, the weak forms and element stiffness matrices of the two formulations are presented. The *Variational Multiscale Method* (VMS) [28] is used to stabilize both formulations, which is required because linear approximations are adopted for all unknowns.

2.3.1. Two-field Formulation – $\mathbf{u}/p$

The mixed $\mathbf{u}/p$ formulation is obtained by substituting the kinematic equation, Eq. (2), and the constitutive equation, Eq. (3), into the balance of momentum equation, Eq. (1). The resulting system of equations reads

$$\nabla \cdot (2\mu_{\text{eff}} \nabla^s \mathbf{u}) + \nabla p + \mathbf{b} = \mathbf{0} \tag{8}$$

$$\nabla \cdot \mathbf{u} = 0. \tag{9}$$

Eq. (8) is the balance of momentum equation in mixed form, defined in terms of both the velocity field $\mathbf{u}$ and the pressure field p. Eq. (9) is the kinematic equation, used to enforce the incompressibility constraint.

Galerkin weak form. The corresponding weak form (after integration by parts) reads

$$\int_\Omega \nabla^s \delta \mathbf{u} \cdot 2\mu_{\text{eff}} \nabla^s \mathbf{u} \, dV + \int_\Omega (\nabla \cdot \delta \mathbf{u}) \, p \, dV + \int_\Omega \delta p \, (\nabla \cdot \mathbf{u}) \, dV = F(\delta \mathbf{u}) \tag{10}$$

where the work of the external loads is

$$F(\delta \mathbf{u}) = \int_\Omega \delta \mathbf{u} \cdot \mathbf{b} \, dV + \int_{\Gamma_t} \delta \mathbf{u} \cdot \bar{\mathbf{t}} \, dA, \tag{11}$$

and where $\delta \mathbf{u}$ and δp are the test functions. Note that the velocity test function vanishes on the boundary $\delta \mathbf{u} = 0$ on Γ_u. The problem is complemented by the Dirichlet and Neumann boundary conditions that are defined as

$$\mathbf{u} = \bar{\mathbf{u}} \quad \text{on} \quad \Gamma_u \tag{12}$$

$$\mathbf{s} \cdot \mathbf{n} = \bar{\mathbf{t}} \quad \text{on} \quad \Gamma_t, \tag{13}$$

where $\bar{\mathbf{u}}$ and $\bar{\mathbf{t}}$ are the prescribed velocities and tractions, respectively, and $\mathbf{n}$ is the unit outward normal to the surface Γ_t.

The discrete Galerkin Finite Element approximation can be obtained by discretizing the computational domain into Finite Elements. The solution of the continuum problem $\{\mathbf{u}, p\}$ is then approximated by $\{\mathbf{u}_h, p_h\}$. The discrete counterpart of the weak form therefore reads

$$\int_{\Omega^e} \nabla^s \delta \mathbf{u}_h \cdot 2\mu_{\text{eff}} \nabla^s \mathbf{u}_h \, dV + \int_{\Omega^e} (\nabla \cdot \delta \mathbf{u}_h) \, p_h \, dV + \int_{\Omega^e} \delta p_h \, (\nabla \cdot \mathbf{u}_h) \, dV = F(\delta \mathbf{u}_h) \tag{14}$$

Stabilization. If the same order of interpolation is used for both velocity and pressure fields, the mixed problem violates the LBB condition [60] and therefore lacks stability. To stabilize the formulation, the Variational Multiscale Method (VMS) is used. The stabilized $\mathbf{u}/p$ formulation reads

$$\int_{\Omega^e} \nabla^s \delta \mathbf{u}_h \cdot 2\mu_{\text{eff}} \nabla^s \mathbf{u}_h \, dV + \int_{\Omega^e} (\nabla \cdot \delta \mathbf{u}_h) \, p_h \, dV + \int_{\Omega^e} \delta p_h \, (\nabla \cdot \mathbf{u}_h) \, dV - \tau_{\mathbf{u}} \int_{\Omega^e} \nabla \delta p_h \cdot \mathsf{P}_h^\perp [\nabla p_h] \, dV = F(\delta \mathbf{u}_h), \tag{15}$$

where $\tau_{\mathbf{u}}$ is a stabilization parameter [29] that is computed as

$$\tau_{\mathbf{u}} = c_u \frac{h^2}{2\mu_{\text{eff}}}. \tag{16}$$

Remark 1. The operator $\mathsf{P}_h^\perp = \mathbf{I} - \mathsf{P}_h$ denotes the projection onto the space orthogonal to the Finite Element space, where P_h is the projection onto the appropriate Finite Element space. Typically the projection P_h is evaluated at the previous iteration and can therefore be moved to the right-hand side of the problem. A detailed derivation of the stabilized mixed $\mathbf{u}/p$ formulation for solid mechanics can be found in [29]. See also [61–63].

Element stiffness matrix. The element-wise approximations of the two-field problem are $\mathbf{u}_h = \mathbf{N}_u \mathbf{U}_h$ and $p_h = \mathbf{N}_p \mathbf{P}_h$ with $\mathbf{U}_h$ and $\mathbf{P}_h$ being the corresponding nodal values of the velocity and pressure fields, respectively. $\mathbf{N}_u$ and $\mathbf{N}_p$ are the matrices of the corresponding shape functions. The Galerkin method defines the test function by using the same shape functions used for the interpolation of the nodal variables, thus $\delta \mathbf{u}_h = \mathbf{N}_u \delta \mathbf{U}_h$ and $\delta p_h = \mathbf{N}_p \delta \mathbf{P}_h$. Thus, the corresponding elemental stiffness matrix reads

$$\mathbf{K} = \int_{\Omega^e} \begin{bmatrix} 2\mu_{\text{eff}} [\mathbf{B}^\mathsf{T} \mathbf{B}] & [\mathbf{G} \mathbf{N}] \\ [\mathbf{N}^\mathsf{T} \mathbf{G}^\mathsf{T}] & -\tau_{\mathbf{u}} [\mathbf{G}^\mathsf{T} \mathbf{G}] \end{bmatrix} dV. \tag{17}$$

2.3.2. Three-field Formulation – $\mathbf{u}/p/\mathbf{e}$

The mixed $\mathbf{u}/p/\mathbf{e}$ formulation is obtained by introducing only the constitutive equation Eq. (3) into the balance of momentum equation Eq. (1) while preserving both the kinematic equation Eq. (2) and the incompressibility constraint Eq. (4).

$$\nabla \cdot (2\mu_{\text{eff}} \mathbf{e}) + \nabla p + \mathbf{b} = \mathbf{0} \tag{18}$$

$$\mathbf{e} - \nabla^s \mathbf{u} = \mathbf{0} \tag{19}$$

$$\nabla \cdot \mathbf{u} = 0 \tag{20}$$

The mechanical problem is now formulated in terms of the deviatoric strain rate $\mathbf{e}$, the pressure p and the velocity $\mathbf{u}$ as primary unknowns.

Galerkin weak form. The corresponding weak form (after integration by parts) reads

$$\int_{\Omega} (\nabla \cdot \delta\mathbf{u}) \cdot p \, dV + \int_{\Omega} \nabla^s \delta\mathbf{u} \cdot 2\mu_{\text{eff}} \mathbf{e} \, dV + \int_{\Omega} \delta p \, (\nabla \cdot \mathbf{u}) \, dV + \int_{\Omega} \delta\mathbf{e} \cdot 2\mu_{\text{eff}} \nabla^s \mathbf{u} \, dV - \int_{\Omega} \delta\mathbf{e} \cdot 2\mu_{\text{eff}} \mathbf{e} \, dV = F(\delta\mathbf{u}), \tag{21}$$

where $\delta\mathbf{u}$, δp and $\delta\mathbf{e}$ are the test functions with $\delta\mathbf{u} = 0$ on Γ_u. Note that the third equation has been multiplied with $2\mu_{\text{eff}}$ to achieve symmetry. The problem is complemented by the same boundary conditions as for the $\mathbf{u}/p$ formulation.

In the corresponding discrete Galerkin Finite Element problem, the solution of the continuum problem $\{\mathbf{u}, p, \mathbf{e}\}$ is now approximated by $\{\mathbf{u}_h, p_h, \mathbf{e}_h\}$.

$$\int_{\Omega^e} (\nabla \cdot \delta\mathbf{u}_h) p_h \, dV + \int_{\Omega^e} \nabla^s \delta\mathbf{u}_h \cdot 2\mu_{\text{eff}} \mathbf{e}_h \, dV + \int_{\Omega^e} \delta p_h \, (\nabla \cdot \mathbf{u}_h) \, dV + \int_{\Omega^e} \delta\mathbf{e}_h \cdot 2\mu_{\text{eff}} \nabla^s \mathbf{u}_h \, dV - \int_{\Omega^e} \delta\mathbf{e}_h \cdot 2\mu_{\text{eff}} \mathbf{e}_h \, dV = F(\delta\mathbf{u}_h) \tag{22}$$

Stabilization. As for the $\mathbf{u}/p$ formulation, the VMS method is adopted to stabilize the formulation. The stabilized $\mathbf{u}/p/\mathbf{e}$ formulation reads

$$\int_{\Omega^e} (\nabla \cdot \delta\mathbf{u}_h) p_h \, dV + \int_{\Omega^e} \nabla^s \delta\mathbf{u}_h \cdot 2\mu_{\text{eff}} \mathbf{e}_h \, dV + \int_{\Omega^e} \delta p_h \, (\nabla \cdot \mathbf{u}_h) \, dV + \int_{\Omega^e} \delta\mathbf{e}_h \cdot 2\mu_{\text{eff}} \nabla^s \mathbf{u}_h \, dV - \int_{\Omega^e} \delta\mathbf{e}_h \cdot 2\mu_{\text{eff}} \mathbf{e}_h \, dV$$
$$+ \tau_{\mathbf{e}} \int_{\Omega^e} \nabla^s \delta\mathbf{u}_h \cdot P_h^{\perp}[2\mu_{\text{eff}} \nabla^s \mathbf{u}_h] \, dV - \tau_{\mathbf{u}} \int_{\Omega^e} \nabla \delta p_h \cdot P_h^{\perp}[\nabla p_h] \, dV = F(\delta\mathbf{u}_h), \tag{23}$$

where the stabilization parameters [46] are computed as

$$\tau_{\mathbf{u}} = c_u \frac{h^2}{2\mu_{\text{eff}}} \tag{24}$$

$$\tau_{\mathbf{e}} = c_e. \tag{25}$$

Remark 2. Analogous to the stabilized $\mathbf{u}/p$ formulation, the stabilization terms for the $\mathbf{u}/p/\mathbf{e}$ also includes projections onto the space orthogonal to the Finite Element space, which also can be moved to the right-hand side of the equation, when evaluated at the previous iteration. For detailed derivation of the stabilized mixed $\mathbf{u}/p/\mathbf{e}$ formulation see [12,46,50].

Element stiffness matrix. The element-wise approximations of the three solution fields are $\mathbf{u}_h = \mathbf{N}_u \mathbf{U}_h$, $p_h = \mathbf{N}_p \mathbf{P}_h$ and $\mathbf{e}_h = \mathbf{N}_e \mathbf{E}_h$ with $\mathbf{U}_h$, $\mathbf{P}_h$ and $\mathbf{E}_h$ being the corresponding nodal values and $\mathbf{N}_u$, $\mathbf{N}_p$ and $\mathbf{N}_e$ being the corresponding matrices of shape functions. The test functions are defined as $\delta\mathbf{u}_h = \mathbf{N}_u \delta\mathbf{U}_h$, $\delta p_h = \mathbf{N}_p \delta\mathbf{P}_h$ and $\delta\mathbf{e}_h = \mathbf{N}_e \delta\mathbf{E}_h$. Thus, the corresponding elemental stiffness matrix reads

$$\mathbf{K} = \int_{\Omega^e} \begin{bmatrix} \tau_{\mathbf{e}} 2\mu_{\text{eff}}[\mathbf{B}^{\mathsf{T}}\mathbf{B}] & [\mathbf{G}\mathbf{N}] & 2\mu_{\text{eff}}[\mathbf{B}^{\mathsf{T}}\mathbf{N}] \\ [\mathbf{N}^{\mathsf{T}}\mathbf{G}^{\mathsf{T}}] & -\tau_{\mathbf{u}}[\mathbf{G}^{\mathsf{T}}\mathbf{G}] & [\mathbf{0}] \\ 2\mu_{\text{eff}}[\mathbf{N}^{\mathsf{T}}\mathbf{B}] & [\mathbf{0}] & -2\mu_{\text{eff}}[\mathbf{N}^{\mathsf{T}}\mathbf{N}] \end{bmatrix} dV. \tag{26}$$

3. Thermal analysis

3.1. Continuum problem

The governing equation of the thermal problem reads

$$\rho_0 c \left(\frac{1}{\alpha} \frac{dT}{dt} + \mathbf{u} \cdot \nabla T \right) + \nabla \cdot \mathbf{q} = D_{\text{m}} \quad \text{with} \quad \mathbf{q} = -k \nabla T, \tag{27}$$

where T is the temperature field (the driving variable of the problem), $\mathbf{u}$ the convective velocity, ρ_0 the material density, c is the (temperature-dependent) specific heat capacity and $\mathbf{q}$ is the heat flux, where k is the (temperature-dependent) thermal conductivity. D_{m} denotes the plastic dissipation (see Section 2.2), acting as source term.

The parameter α is introduced to artificially accelerate the transient phase by increasing the thermal diffusion. Thus, the steady state condition can be achieved faster. This method was first introduced by Dialami et al. [64] for the numerical simulation of FSW processes.

3.2. Finite element formulation

The corresponding weak form of the thermal problem reads

$$\int_{\Omega} \delta T \, \rho_0 c \left(\frac{1}{\alpha} \frac{dT}{dt} + \mathbf{u} \cdot \nabla T \right) dV + \int_{\Omega} \nabla \delta T \cdot k \nabla T \, dV = \int_{\Omega} \delta T \cdot D_{\text{m}} \, dV - \int_{\Gamma_q} \delta T \cdot \bar{q} \, dA, \tag{28}$$

where δT is the test function of the temperature field.

The problem is complemented by the boundary conditions. The boundary Γ of Ω is split into Γ_T, where the prescribed temperatures $\bar{T}$ are specified (Dirichlet boundary conditions), and Γ_q, where the prescribed heat fluxes $\bar{q}$ are applied (Neumann boundary conditions), such that $\Gamma_T \cup \Gamma_q = \Gamma$ and $\Gamma_T \cap \Gamma_q = \emptyset$. The boundary conditions are defined as

$$T = \bar{T} \quad \text{on} \quad \Gamma_T \tag{29}$$

$$\mathbf{q} \cdot \mathbf{n} = \bar{q} \quad \text{on} \quad \Gamma_q, \tag{30}$$

where $\mathbf{n}$ is the unit outward normal to the surface Γ_q. On surfaces which are in contact with the back plate, the heat is dissipated by conduction and can be expressed by Newton's law as

$$q_{\mathrm{cond}} = h_{\mathrm{cond}}(T - T_{\mathrm{backplate}}), \tag{31}$$

where h_{cond} is the heat transfer coefficient by conduction and $T_{\mathrm{backplate}}$ the environment temperature. Heat fluxes to the environment by convection and radiation are not considered. The initial temperature for the transient thermal problem is $T(t = 0) = T_0$.

The discrete Galerkin Finite Element approximation can be obtained by discretizing the computational domain into Finite Elements. The solution of the continuum problem T is now approximated by T_h. Thus, the discrete counterpart of the weak form reads

$$\int_{\Omega^e} \delta T_h \, \rho_0 c \left(\frac{1}{\alpha} \frac{dT_h}{dt} + \mathbf{u}_h \cdot \nabla T_h \right) dV + \int_{\Omega^e} \nabla \delta T_h \cdot k \nabla T_h \, dV = \int_{\Omega^e} \delta T_h \, D_{\mathrm{m}} \, dV - \int_{\Gamma_q^e} \delta T_h \, \bar{q} \, dA. \tag{32}$$

Remark 3. The Eulerian formulation, adopted for the mechanical problem, introduces convection terms in the governing equations of the thermal problem. In convection dominated problem this may cause stability problems. In this work, Galerkin Least-Squares (GLS) stabilization is used to stabilize the thermal problem [65].

Remark 4. The coupled thermo-mechanical problem is solved through a staggered scheme derived from a fractional step method [1]. Thus, the mechanical problem is solved first, based on the current temperature field. Next, the thermal field is computed, based on the updated velocity field. Note that the mechanical problem requires temperature-dependent material properties (i.e., the viscosity and flow index), while the thermal problem requires the velocity field $\mathbf{u}$ to compute the convection term and the mechanical dissipation D_{m} as heat source.

4. Adaptive formulation refinement

In order to define a most suitable and computationally efficient framework for an FSW simulation, the adaptive use of both the two- and three-field formulations is proposed in this work. The AFR method switches between the $\mathbf{u}/p$ and $\mathbf{u}/p/\mathbf{e}$ formulations, driven by a refinement criterion based on a posteriori error estimation.

When compared to established refinement approaches (i.e., adaptive h- and p-refinement), the AFR method shows some advantages which are beneficial for simulating FSW problems. By using a stabilized mixed formulation, linear interpolation can be adopted for all variable fields. Moreover, the same mesh is used during the whole analysis, thus no remeshing is required. Finally, the treatment of the interface between refined and unrefined subdomains is straightforward since no hanging nodes need to be considered. The AFR approach can be broken down into four parts:

1. Definition of an a posteriori error estimator, to drive the adaptive method
2. Strain rate and stress consistency
3. Definition of the adaptivity approach
4. Integration into a High Performance Computing (HPC) framework

4.1. Refinement criteria and error estimation

For some applications it is possible to know a priori where a high accuracy is required. Thus, a finer mesh, a different formulation or higher order shape functions, can be set at the beginning of the simulation. However, this is typically not known a priori and adaptive approaches are used instead. As a consequence, a posteriori error estimators and refinement criteria are used to determine where the highest errors occur and refinement is required. For the AFR approach, this means determining where to use the $\mathbf{u}/p$ and $\mathbf{u}/p/\mathbf{e}$ formulations, respectively.

In the present work, the well known Zienkiewicz–Zhu (ZZ) error estimator [52] is used. The local (element-wise) error e_{ZZ} is estimated by comparing two strain rates ($\mathbf{e}_{\mathrm{p}}$ and $\mathbf{e}_{\mathrm{c}}$) at the center of the element. The first strain rate $\mathbf{e}_{\mathrm{p}}$ is obtained by computing the symmetric gradient of the velocity at the integration points, projecting them to the nodes using a lumped mass matrix projection and interpolating the results to the center of the element. The second strain rate $\mathbf{e}_{\mathrm{c}}$ is computed as the symmetric gradient of the velocity field directly at the center of the element without projecting it to the nodes first. Subsequently, the difference is computed as $\mathbf{e}_{\mathrm{diff}} = \mathbf{e}_{\mathrm{p}} - \mathbf{e}_{\mathrm{c}}$ and the norm of the strain rate difference is integrated over the element according to Eq. (33).

$$e_{ZZ} = \int_{\Omega^e} \mathbf{e}_{\mathrm{diff}} : \mathbf{e}_{\mathrm{diff}} \, d\Omega^e \tag{33}$$

For Finite Element approaches with C^0 continuity, this error estimator approximately quantifies the difference between the strain rate field obtained by computing the symmetric gradient of the velocity field in the $\mathbf{u}/p$ formulation and the strain rate field that would be obtained by using the $\mathbf{u}/p/\mathbf{e}$ approach. Hence, it is a good indicator to switch from $\mathbf{u}/p$ to $\mathbf{u}/p/\mathbf{e}$.

4.2. Strain rate and stress consistency

This subsection aims to explain how strain rates and stresses are obtained in the different mixed formulations. This is important to later ensure a consistency of those fields at the interface between unrefined ($\mathbf{u}/p$) and refined ($\mathbf{u}/p/\mathbf{e}$) subdomains.
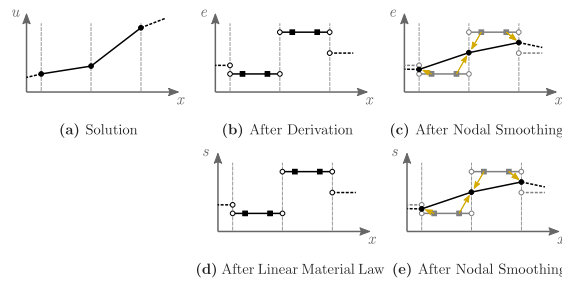
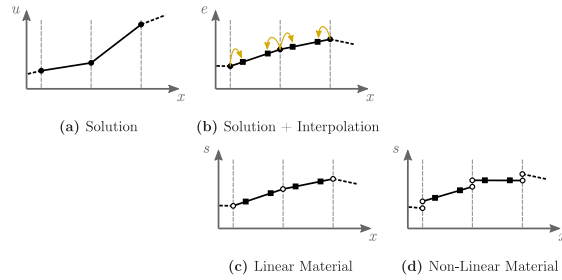**Fig. 3.** Strain rate and stress handling in two-field $\mathbf{u}/p$ formulation.

Fig. 4. Strain rate and stress handling in three-field $\mathbf{u}/p/\mathbf{e}$ formulation.

$\mathbf{u}/p$ *formulation.* In the two-field formulation, the velocity field $\mathbf{u}$ is computed at the nodes (●, Fig. 3(a)). Assuming linear elements, the resulting field is therefore C^0-continuous. To obtain the strain rate $\mathbf{e}$, the first derivative is computed at the integration points (■) of the elements (Fig. 3(b)). Due to the derivation, the strain rate field becomes C^{-1}-continuous or *discontinuous*. This is especially obvious for linear simplex elements since the strain rate is constant within each element. Finally the stresses are obtained (Fig. 3(d)) by evaluating the material law. Since the strain rates are computed and stored at the integration points, the material law is also evaluated at the integration points. Therefore, both the stresses and the mechanical dissipation are computed at the same location. To postprocess the strain rate, stress or dissipation, the fields are often projected onto the nodes (Figs. 3(c) and 3(e)) in order to show continuous fields.

$\mathbf{u}/p/\mathbf{e}$ *formulation.* Unlike in the two-field formulation, the strain rate is now considered an additional primary unknown and is therefore defined at the nodes. (Fig. 4(b)). This given, two different approaches could be followed.

The first approach would be to also compute stresses and the dissipation at the nodes. However, this would require to evaluate the material law at the nodes, which is possible but uncommon. It would also create an inconsistency between the $\mathbf{u}/p$ and $\mathbf{u}/p/\mathbf{e}$ subdomains.

To keep consistency between the $\mathbf{u}/p$ and $\mathbf{u}/p/\mathbf{e}$ subdomains, the same approach as for the two-field formulation is followed. The strain rate field is available at the nodes (●), hence it is C^0-continuous. Afterwards the field is interpolated to the integration points (■, Fig. 4(b)) and thus it is still continuous. Considering a linear material law, also the stresses are continuous (Fig. 4(c)). Only when considering a non-linear material law, a discontinuous stress field can be observed (Fig. 4(d)). Finally, the mechanical dissipation, which is computed from the stresses and the strain rate, can also be easily computed at the integration points.

4.3. Adaptive approach

At the beginning of each time step, the evaluation of the refinement criterion (based on the chosen error estimator) yields the definition of the $\mathbf{u}/p$ and $\mathbf{u}/p/\mathbf{e}$ subdomains. The element stiffness matrices are then computed according to which subdomain the current element belongs to. Since the $\mathbf{u}/p$ formulation is a subset of the $\mathbf{u}/p/\mathbf{e}$ formulation, it is convenient to consider the three-field formulation as the default approach. Thus, in the $\mathbf{u}/p$ subdomain the degrees of freedom associated with the strain rate are deactivated.

At the interface between the $\mathbf{u}/p$ and $\mathbf{u}/p/\mathbf{e}$ elements all three-field variables ($\mathbf{u}$, p and $\mathbf{e}$) are preserved. A schematic representation of the interface between two-field and three-field elements can be seen in Fig. 5. Note that all nodes at the interface are $\mathbf{u}/p/\mathbf{e}$ nodes.

Thanks to the unified way of treating the strain rate, the *mixed* strain rate field can be obtained straightforwardly, as seen in Fig. 6. In the $\mathbf{u}/p$ subdomain the strain rate is obtained by computing the symmetric gradient of the velocity at the integration points, whereas in the $\mathbf{u}/p/\mathbf{e}$ subdomain, the strain rate is directly obtained as a solution at the nodes and afterwards interpolated to the
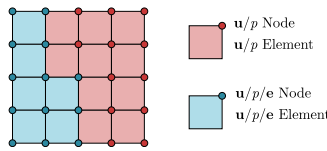
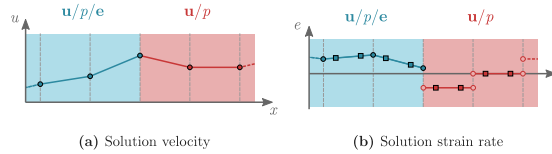**Fig. 5.** Interface of **u**/p/**e** and **u**/p elements and nodes.

(a) Solution velocity   (b) Solution strain rate

Fig. 6. Solution fields at the formulation interface.

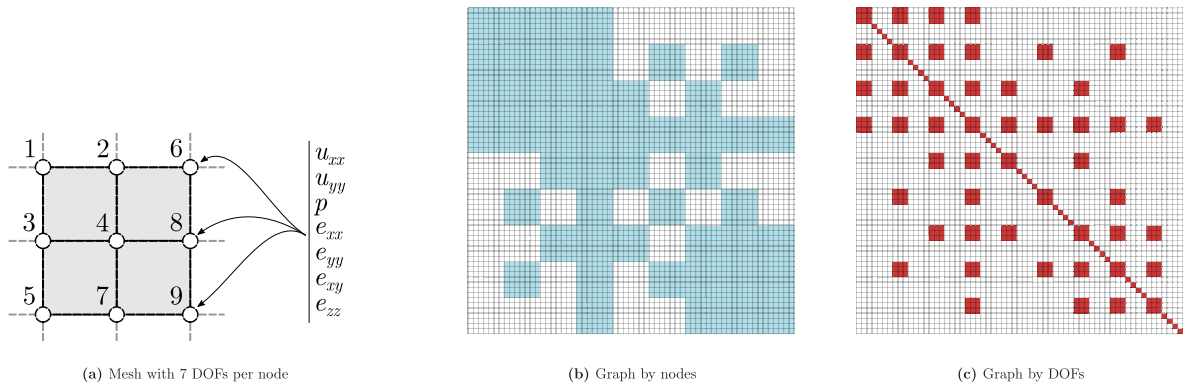(a) Mesh with 7 DOFs per node   (b) Graph by nodes   (c) Graph by DOFs

Fig. 7. Visualization of non-zero matrix entries of an AFR problem.

integration points. Therefore, the subsequent computation of the stresses and the dissipation can be carried out at the integration points.

Remark 5. Special attention must be paid to the computation of the strain rate subscales when using orthogonal sub-grid stabilization (OSS, a specific type of VMS stabilization [29,61]). The computation of the projection onto the space of subscales $\tilde{\mathrm{P}}$ involves the nodal projection of the subscales of the affected variables. This poses no problem for the velocity and pressure subscales since both fields are defined on the whole domain. The strain rate subscales, however, only exist in the **u**/p/**e** subdomain. Consequently, the nodes at the interface between the **u**/p and **u**/p/**e** subdomains lack a contribution from adjacent **u**/p elements, when the nodal projection of the strain rate subscales is performed. To solve this problem the nodal strain rate in the **u**/p subdomain is approximated by a nodal projection of the symmetric gradient of the velocity.

4.4. Solver strategies

The purpose of the deactivation of the degrees of freedom (DOFs) associated to the strain rate in the **u**/p subdomain is to create a problem which is smaller (less required memory) and faster to solve (less required CPU-time). However, to achieve this, some aspects of the deactivation process requires further discussion.

In most Finite Element codes, the system matrices are usually stored in a compressed format like the *Compressed Sparse Row* (CSR) format. The graph of the matrix is used to locate an entry of the matrix. Note that the graph only accounts for non-zero entries of the matrix.

In the following, the small mesh shown in Fig. 7(a) is analyzed. In most Finite Element applications all nodes have the same number of DOFs and almost all assembled values are non-zeros. In such cases it is convenient to build the graph by nodes. This allows all DOFs associated with a particular node to be assembled in a single operation. The resulting pattern of non-zeros is shown in Fig. 7(b).

In the context of the AFR method, the mesh shown in Fig. 7(a) could correspond to a **u**/p subdomain. Hence, only the velocity and pressure DOFs are of interest. However, if no further action is taken, the graph and pattern of non-zeros would remain the same as the one corresponding to the default **u**/p/**e** formulation. This causes two problems. First, a large number of zeros are assembled

```
-ksp_type bcgs
-ksp_rtol 1e-8
-ksp_max_it 300
-ksp_diagonal_scale
```

Fig. 8. PETSc solver settings. Note that the maximum number of solver iterations specified (300) is never reached. The default preconditioning in PETSc is ILU(0).

to the system, which is increasing the build time unnecessarily. Second, although the assembled zeros do not contribute to the solution, the solver needs to consider these entries when solving the system because – according to the graph – they are considered non-zeros. This increases the solve time.

The solution to this problem is to build the graph by DOFs. This allows to only consider the $\mathbf{u}/p$ DOFs as well as a unitary value in the positions of the main diagonal which correspond to strain rate components as part of the graph and therefore as non-zero entries. Hence, the latter do not contribute noticeably to the solving time since they are the only non-zero entries in their respective rows and columns. This results in faster build and solve times and avoids any renumbering of the DOFs since all matrices remain the same size.

The resulting pattern of non-zeros is shown in Fig. 7(c).

Remark 6. The activation and deactivation of DOFs is handled at runtime. For each time step the refinement criterion is evaluated and the elements (and respective nodes) are determined to be either $\mathbf{u}/p/\mathbf{e}$ or $\mathbf{u}/p$. The DOF graph is then modified correspondingly.

Remark 7. The authors of the present paper use the PETSc library [66] to build and solve the system. In PETSc, the expression 'BAIJ-matrix' (*B* stands for '*blocked*') refers to matrices that support multiple DOFs being assembled as one block in a single operation (i.e., the graph is built by nodes). In the example shown in Fig. 7(a), the block size is 7 (the number of DOFs per node), and must be the same for all nodes. To be able to vary the number of DOFs per node, the graph must be built by DOFs. Therefore, in PETSc, an 'AIJ-matrix' must be used instead.

5. Numerical examples

In this section the proposed AFR method is assessed by solving several numerical examples. Four different examples are shown, each giving a different perspective on the performance of the presented method.

Example 1 The build and solve times for different matrix types and assembly strategies are studied. This example assesses the results obtained with the PETSc solver library.

Example 2 A simple 2D *flow over a cylinder* case is presented. This example shows the dissipation field for the $\mathbf{u}/p$ and $\mathbf{u}/p/\mathbf{e}$ formulations, as well as the solution using AFR. The solution accuracy in different parts of the domain is assessed with regard to the different formulations.

Example 3 A global error analysis is performed in order to study the convergence rates upon mesh refinement and to prove that the AFR method converges to the analytical solution. Furthermore, the influence of the arrangement of $\mathbf{u}/p$ and $\mathbf{u}/p/\mathbf{e}$ subdomains is studied.

Example 4 Finally, an FSW application is presented. The example is a 3D, thermo-mechanically coupled case with highly non-linear material behavior. This final example aims to demonstrate the use of the AFR method for industrial applications.

In all examples, the stabilization coefficients (see Eqs. (17) and (26)) are $c_u = 1.0$ and $c_e = 0.1$ for both the $\mathbf{u}/p$ and $\mathbf{u}/p/\mathbf{e}$ formulations.

5.1. Build and solve times assessment

To measure the build and solve times, a 3D case consisting of 70 490 nodes and 66 470 hexahedral elements, is studied for different formulations and matrix types. In the $\mathbf{u}/p$ cases, this resulted in building and solving a system with 281 960 unknowns (number of nodes times 4 DOF: u_x, u_y, u_z, p) and in $\mathbf{u}/p/\mathbf{e}$ and AFR cases, a system with 704 900 unknowns (number of nodes times 10 DOF: u_x, u_y, u_z, p, e_{xx}, e_{yy}, e_{zz}, e_{xy}, e_{xz}, e_{yz}). A single iteration is carried out in parallel (6 Threads) on an Intel Core i7-10750H CPU. For this analysis, the PETSc implementation of the stabilized version of the biconjugate gradient method (BCGS) is used, with the settings shown in Fig. 8.

The build and solve times for two different matrix types (AIJ and BAIJ) and assembly strategies (node graph and DOF graph), as introduced in Section 4.4, are shown in Table 1. In the first section (labeled *genuine formulation*, Nos. 1 and 2) no DOFs are activated nor deactivated. Only the straightforward implementations of the $\mathbf{u}/p$ and $\mathbf{u}/p/\mathbf{e}$ formulations are used. In both cases the

Table 1
Build and solve times for different methods and matrix types.

No.	Method, Matrix type, Graph type		Unknowns	Build time	Solve time
1	genuine formulation, BAIJ, node graph	$\mathbf{u}/p$	281 960	0.85 s	7.75 s
		$\mathbf{u}/p/\mathbf{e}$	704 900	3.15 s	62.97 s
2	genuine formulation, AIJ, node graph	$\mathbf{u}/p$	281 960	1.05 s	10.02 s
		$\mathbf{u}/p/\mathbf{e}$	704 900	4.98 s	71.65 s
3	AFR method, AIJ, node graph	$\mathbf{u}/p$	704 900	3.31 s	54.58 s
		$\mathbf{u}/p/\mathbf{e}$	704 900	4.72 s	73.21 s
4	AFR method, AIJ, DOF graph	$\mathbf{u}/p$	704 900	→ 1.75 s	→ 12.30 s
		$\mathbf{u}/p/\mathbf{e}$	704 900	4.72 s	71.66 s
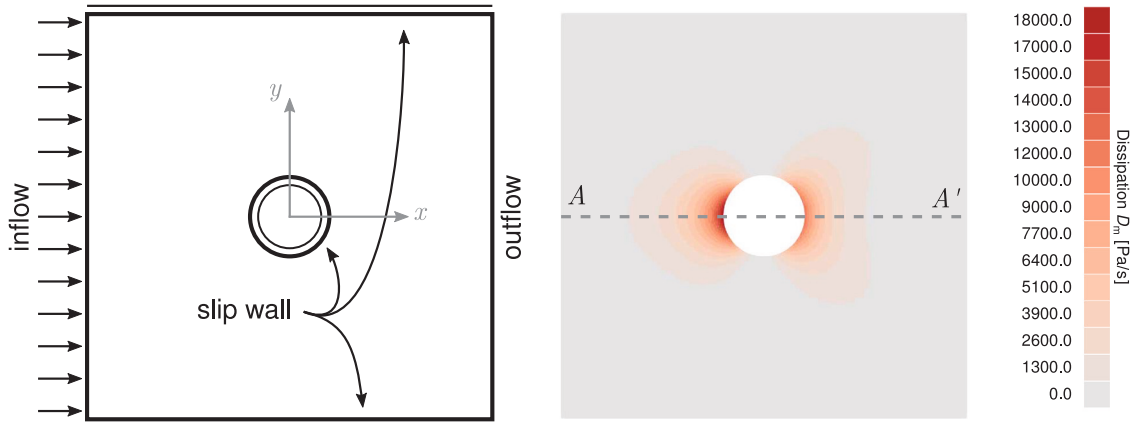
Fig. 9. Flow over a cylinder: analysis of dissipation.

graph was built by nodes. The build and solve times of the genuine formulations indicate the range in which the times of the AFR method should fall. Considering the solve times first, the lower bound is set by the genuine $\mathbf{u}/p$ formulation with 7.75 s and 10.02 s for the BAIJ and AIJ matrices, respectively. The upper bound is set by the genuine $\mathbf{u}/p/\mathbf{e}$ formulation with 62.97 s and 71.65 s, respectively. As expected, it takes more time to solve the $\mathbf{u}/p/\mathbf{e}$ problem than the $\mathbf{u}/p$ problem and that both building and solving are faster if BAIJ matrices are used.

The second section (Nos. 3 and 4) shows the results obtained by using the AFR method. This means that the system is always of the size of the corresponding $\mathbf{u}/p/\mathbf{e}$ problem and in the $\mathbf{u}/p$ cases, the DOFs associated with the strain rate were not assembled. The goal of using the AFR method is to achieve build and solve times that are as close as possible to those of the genuine $\mathbf{u}/p$ formulation, despite dealing with a system of the size of the $\mathbf{u}/p/\mathbf{e}$ problem.

This is possible when the AFR method uses an AIJ matrix in order to take advantage of the DOF graph (No. 4). The performance of the AFR method can be assessed by comparing the $\mathbf{u}/p$ (AIJ) times of the AFR method (No. 4, 12.30 s) to the $\mathbf{u}/p$ (AIJ) and $\mathbf{u}/p/\mathbf{e}$ (AIJ) times of the genuine formulations (10.02 s and 71.65 s). The AFR method is only marginally slower than the genuine $\mathbf{u}/p$ formulation, despite solving a system with 2.5 times as many unknowns.

The necessity of using a DOF graph instead of a node graph becomes obvious when comparing the AFR times for different graph types (Nos. 3 and 4): 12.30 s vs. 54.58 s.

Note that the build and solve times of the $\mathbf{u}/p/\mathbf{e}$ problem do not vary significantly between Nos. 2 to 4. This shows that the implementation of the AFR method does not introduce any notable computational overhead when dealing with a *full* problem where all possible DOFs are active.

Using a graph based on the active DOFs results in a faster solution times compared to the original node-based graph. The build times follow a similar pattern, though for big problems the solving time dominates the overall required CPU-time.

5.2. Local error analysis

The second example assesses the local solution of a 2D *flow-over-a-cylinder* case. The geometry and boundary conditions are shown in Fig. 9. The square domain is of size 10 m × 10 m and the cylinder located in the center of the domain has a diameter of 2 m. The inflow velocity is set to $u_x = 0.01$ ms^{-1}. The top and bottom boundaries as well as the boundary of the cylinder are modeled as *slip wall* conditions, thus the tangential velocity is free and the normal velocity is set to $u_n = 0$. This example is purely mechanical (temperature coupling is not accounted for) and adopts linear material behavior (Newtonian law). The material viscosity is set to $\mu_0 = 1 \cdot 10^8$ Pa s and the flow index to $m = 1$.
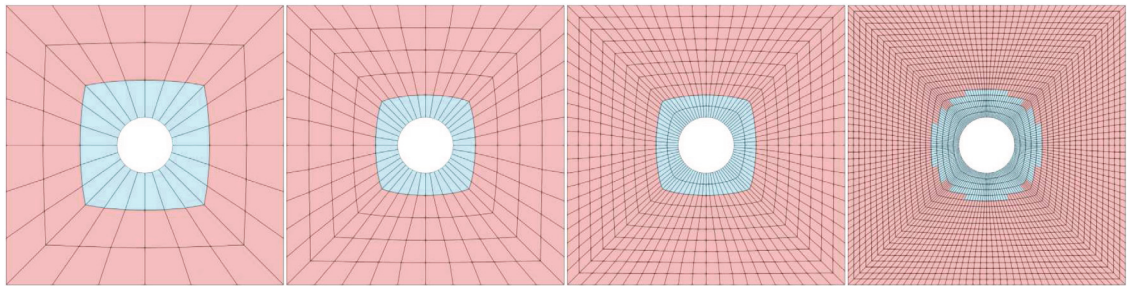
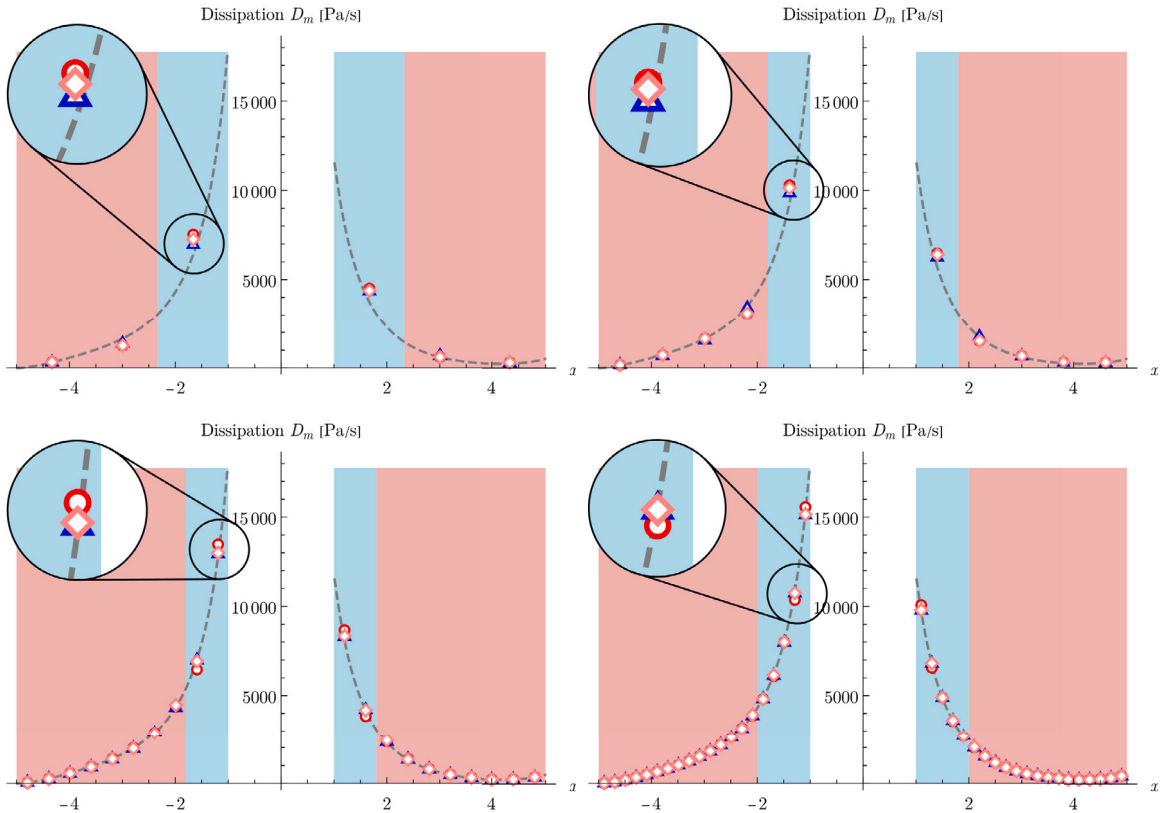**Fig. 10.** Differently fine meshes: 96, 240, 880 and 3360 nodes.

Fig. 11. Dissipation over line $A - A'$ for different mesh resolutions: reference solution indicated by dashed line, ○ $\mathbf{u}/p$, △ $\mathbf{u}/p/\mathbf{e}$ and ◇ AFR.

Fig. 9 shows a plot of the dissipation D_{m} on a very fine (120 800 nodes) reference mesh. Fig. 11 shows line plots ($A - A'$) of the dissipation for four gradually finer meshes (see Fig. 10). The dashed line indicates the reference solution as seen in Fig. 9. The different markers indicate the solution of the $\mathbf{u}/p$ formulation (○), the $\mathbf{u}/p/\mathbf{e}$ formulation (△) and the AFR method (◇). In the case of the AFR method, the different subdomains are indicated by the background color: light red for the $\mathbf{u}/p$ subdomain and light blue for the $\mathbf{u}/p/\mathbf{e}$ subdomain. These subdomains were created a priori.

Far from the cylinder axis, where smaller dissipation values are expected, all three methods give very similar results, matching the reference solution. However, the dissipation field close to the cylinder shows a larger deviation from the reference solution. This deviation is always higher for the $\mathbf{u}/p$ formulation and is always lower for the $\mathbf{u}/p/\mathbf{e}$ formulation.

For all four meshes, the solution of the AFR strategy is located between the solution of the $\mathbf{u}/p$ and $\mathbf{u}/p/\mathbf{e}$ formulations. For the two coarser meshes, where only a single element is part of the $\mathbf{u}/p/\mathbf{e}$ subdomain, the solutions of the AFR strategy is closer to the $\mathbf{u}/p$ solution. Whereas, if more than one element belongs the $\mathbf{u}/p/\mathbf{e}$ subdomain, the AFR solution is almost identical to the $\mathbf{u}/p/\mathbf{e}$ solution.
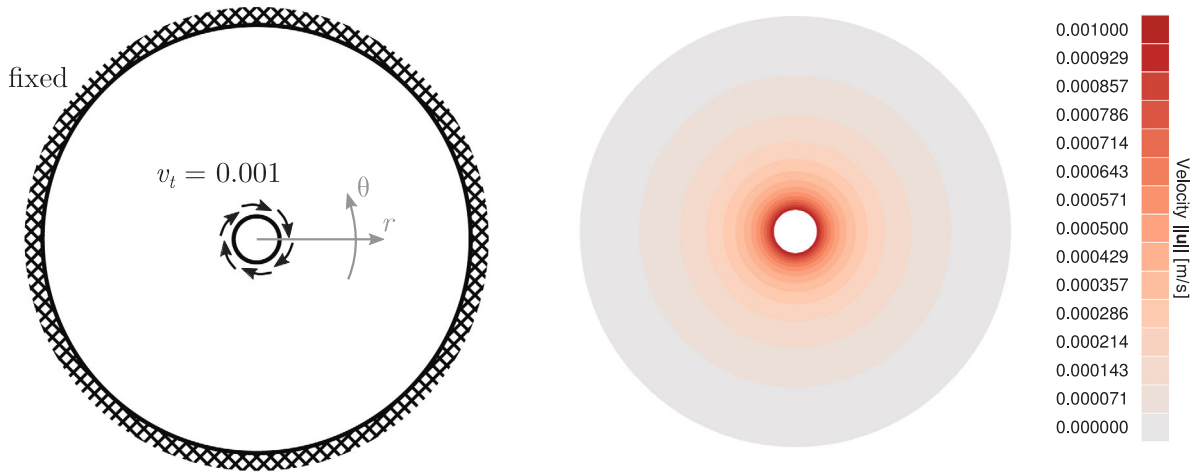
Fig. 12. Flow around cylinder: analytical solution of velocity norm ‖**u**‖.

The outcome is the following: (1) in low dissipation areas, all three formulations yield similar results, (2) the AFR solution seems to be bounded by the **u**/p and **u**/p/**e** solutions and (3) if the **u**/p/**e** subdomain is sufficiently large, the AFR solution tends towards the **u**/p/**e** solution.

5.3. Global error analysis

In this example a convergence study upon mesh refinement is carried out. In the present study, the convergence rates of the velocity **u** and the energy e are examined. The norms of the errors [67] are obtained as follows

$$\|\mathbf{u} - \mathbf{u}_h\| = \left[\int_{\Omega} (\mathbf{u} - \mathbf{u}_h) : (\mathbf{u} - \mathbf{u}_h)\, \mathrm{d}\Omega\right]^{1/2} \tag{34}$$

$$\|e - e_h\| = \left[\int_{\Omega} (\mathbf{s} - \mathbf{s}_h) : (\mathbf{e} - \mathbf{e}_h)\, \mathrm{d}\Omega\right]^{1/2}, \tag{35}$$

where **u** is the velocity and **s** and **e** are the deviatoric stresses and strains in Voigt notation, respectively. The index $\square_h$ indicates the Finite Element approximation.

The geometry and boundary conditions are presented in Fig. 12. The circular domain has an outer diameter of 20 m and an inner diameter of 2 m. Homogeneous Dirichlet boundary conditions are applied to the outer perimeter of the circular domain. The inner perimeter is subjected to a prescribed velocity in tangential direction of $u_{\theta} = 0.001$ m/s. The resulting velocity field can be observed in Fig. 12. The example is purely mechanical (the temperature coupling was not modeled) and linear material behavior is adopted (Newtonian law). The material viscosity is set to $\mu_0 = 1$ Pa s and the flow index to $m = 1$.

For the given geometry and boundary conditions, the analytical solution is used to compute a global error in terms of the velocity field, its spacial derivatives and the pressure field:

$$u_r = 0 \qquad\qquad u_{\theta} = -\frac{-100 + r^2}{99\,000\, r} \tag{36}$$

$$u_{r,r} = u_{r,\theta} = u_{\theta,\theta} = 0 \quad u_{\theta,r} = -\frac{100 + r^2}{99\,000\, r^2} \tag{37}$$

$$p = \text{const.} \tag{38}$$

The AFR strategy relies on optimizing the use of the **u**/p and **u**/p/**e** subdomains according to an error criterion. For the given example, the **u**/p/**e** formulation should be used close to the circular hole in the middle of the domain. The convergence study assesses the convergence rates for three differently subdivided domains and compares the results of the AFR method to the **u**/p and **u**/p/**e** formulations.

Fig. 13(a) shows a reasonable subdivision scheme, where the **u**/p/**e** subdomain is close to the center of the whole domain, whereas Figs. 13(b) and 13(c) depict two unreasonable subdivision schemes.

To assess the convergence rates, the global error is plotted over the mesh size h and the total number of degrees of freedom. Figs. 14 and 15 show the velocity error ‖**u** − **u**_h‖ for different subdivision schemes, while Figs. 16 and 17 show the energy norm error ‖$e − e_h$‖. All plots show the **u**/p (■) and **u**/p/**e** (■) results as reference.

It can be clearly seen from Figs. 14 and 15, that the velocity error ‖**u** − **u**_h‖ decreases with the same convergence rate for all formulations. Though, for a given mesh size h, the **u**/p/**e** solution (■), as well as the AFR solution with the reasonable subdivision
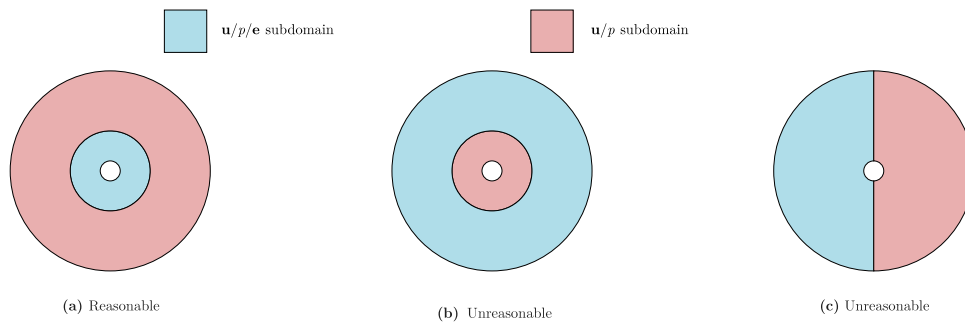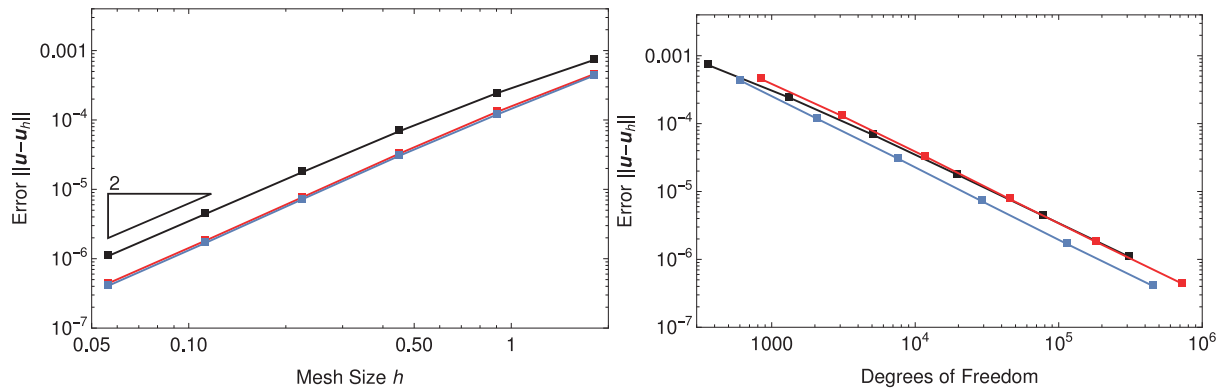
Fig. 13. Different strategies to divide the domain in $\mathbf{u}/p$ and $\mathbf{u}/p/\mathbf{e}$ subdomains.

Fig. 14. Velocity errors $\|\mathbf{u} - \mathbf{u}_h\|$ for different subdivision schemes: ■ $\mathbf{u}/p/\mathbf{e}$, ■ $\mathbf{u}/p$ and ■ AFR (reasonable, Fig. 13(a)).
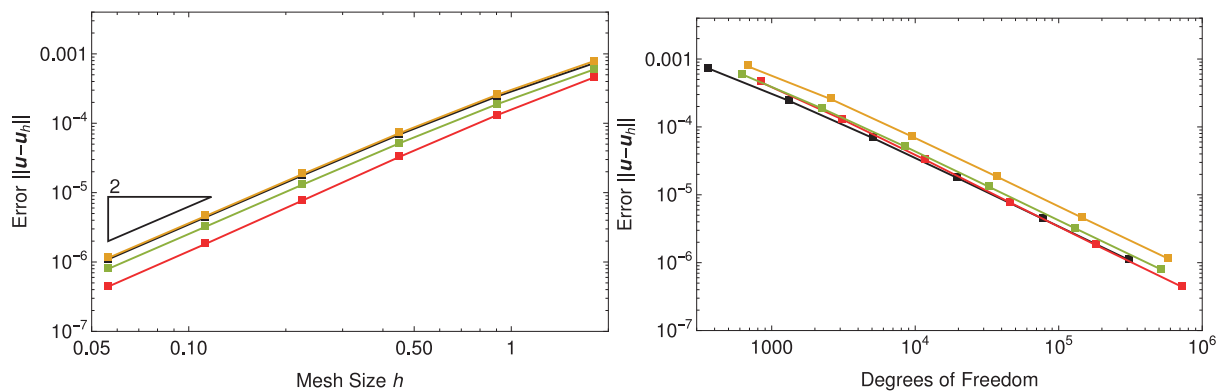
Fig. 15. Velocity errors $\|\mathbf{u} - \mathbf{u}_h\|$ for different subdivision schemes: ■ $\mathbf{u}/p/\mathbf{e}$, ■ $\mathbf{u}/p$, ■ AFR (unreasonable, Fig. 13(b)) and ■ AFR (unreasonable, Fig. 13(c)).

scheme (■), yield more accurate results. However, if the error is displayed over the number of DOFs, the AFR solution (■) always yields the highest accuracy for a given number of DOFs. As expected, the AFR solutions using the unreasonable subdomains (■, ■) perform worse than the $\mathbf{u}/p$ formulation (■): for the same accuracy they require a higher number of DOFs.

A different behavior can be observed, when the error is studied using the energy norm $\|e - e_h\|$, as shown in Figs. 16 and 17. It can be observed that the $\mathbf{u}/p/\mathbf{e}$ formulation (■) yields both the highest convergence rate and the most accurate results, while the $\mathbf{u}/p$ formulation (■) yields both the lowest convergence rate and the worst accuracy. The results (accuracy and convergence rate) obtained by the AFR technique are bounded by the results of the $\mathbf{u}/p$ and $\mathbf{u}/p/\mathbf{e}$ formulations. The two unreasonable subdivision schemes (■, ■) perform as bad as the $\mathbf{u}/p$ formulation (or slightly better) while the reasonable subdivision scheme (■) performs almost as good as the $\mathbf{u}/p/\mathbf{e}$ formulation. Only for very small mesh sizes, the convergence rate of the reasonable subdivision scheme (■) shifts towards the $\mathbf{u}/p$ behavior. This is expected, as for very fine meshes, the error of the $\mathbf{u}/p$ subdomain begins to dominate
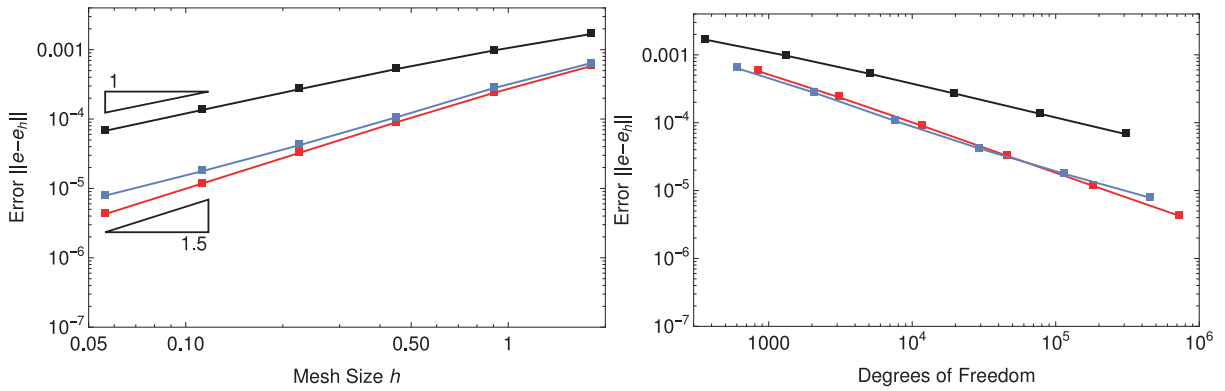
Fig. 16. Energy norm errors $\|e - e_h\|$ for different subdivision schemes: ■ $\mathbf{u}/p/\mathbf{e}$, ■ $\mathbf{u}/p$ and ■ AFR (reasonable, Fig. 13(a)).
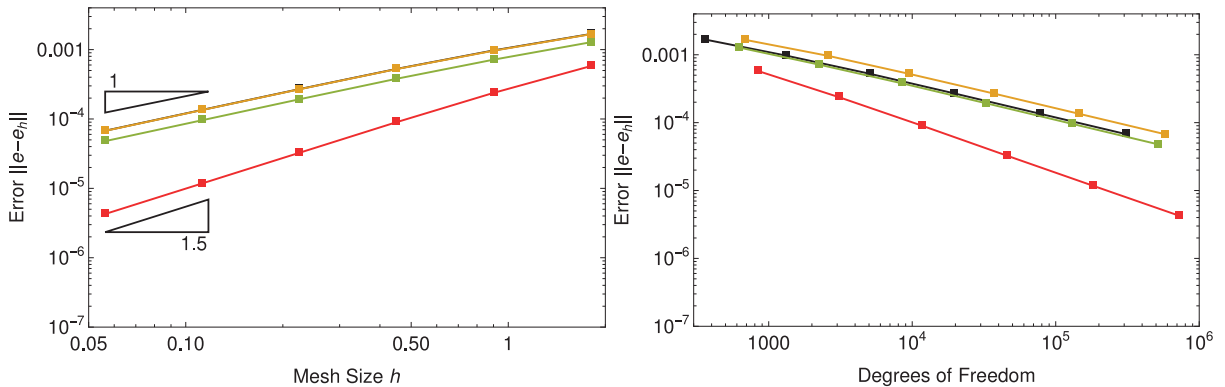
Fig. 17. Energy norm errors $\|e - e_h\|$ for different subdivision schemes: ■ $\mathbf{u}/p/\mathbf{e}$, ■ $\mathbf{u}/p$, ■ AFR (unreasonable, Fig. 13(b)) and ■ AFR (unreasonable, Fig. 13(c)).

the general convergence behavior. When displaying the error in the energy norm over the number of DOFs, it can be observed that the AFR technique performs as good as the $\mathbf{u}/p/\mathbf{e}$ formulation, if a reasonable subdivision scheme is adopted.

Therefore, the initial findings of the local error analysis are confirmed: the results obtained using the AFR method are bounded by the $\mathbf{u}/p$ and $\mathbf{u}/p/\mathbf{e}$ formulations. Furthermore it is proven that the method converges towards the correct solution upon mesh refinement. The results also show that a reasonable choice of $\mathbf{u}/p$ and $\mathbf{u}/p/\mathbf{e}$ subdomains is important. The three-field formulation is most appropriate when large gradients are expected.

5.4. Friction stir welding application

The final example is selected to show that the AFR strategy can be employed for industrial applications. For the sake of simplicity, the geometric complexity of the actual pin-tool (e.g., threading and tilting, which is generally tackled with ALE or embedded formulations) is avoided. Only the large strain rate gradient in the thermo-mechanically affected zone is retained in the proposed analysis. Thus, a simpler cylindrical pin-tool is assumed to show the advantages and the accuracy of the AFR method.

Next, the following aspects of the analysis are described: (1) the description of the geometry and the corresponding mesh, (2) the loading and boundary conditions, (3) an overview of the temperature-dependent material parameters and (4) the obtained Finite Element results as well as an assessment of the influence of the AFR technique on the solution.

5.4.1. Geometry and mesh

The work pieces (the metal sheets to be welded) are modeled as flat hexahedral domains in an Eulerian framework, with a cylindrical hole, as shown in Fig. 18. The computational domain for the sheet is of size 100 mm × 100 mm with a thickness of 7 mm. The pin has a diameter of 6 mm and is inserted into the sheet to a depth of 6 mm. The tool shoulder has a diameter of 16 mm and is in contact with the sheet. The structured mesh consists of 122 425 nodes and 114 516 linear, hexahedral elements. When the $\mathbf{u}/p$ formulation is used in the entire domain, the problem consists of approximately 500 000 DOFs. Using the $\mathbf{u}/p/\mathbf{e}$ formulation everywhere, the total number of DOFs is approximately 1.2 million.
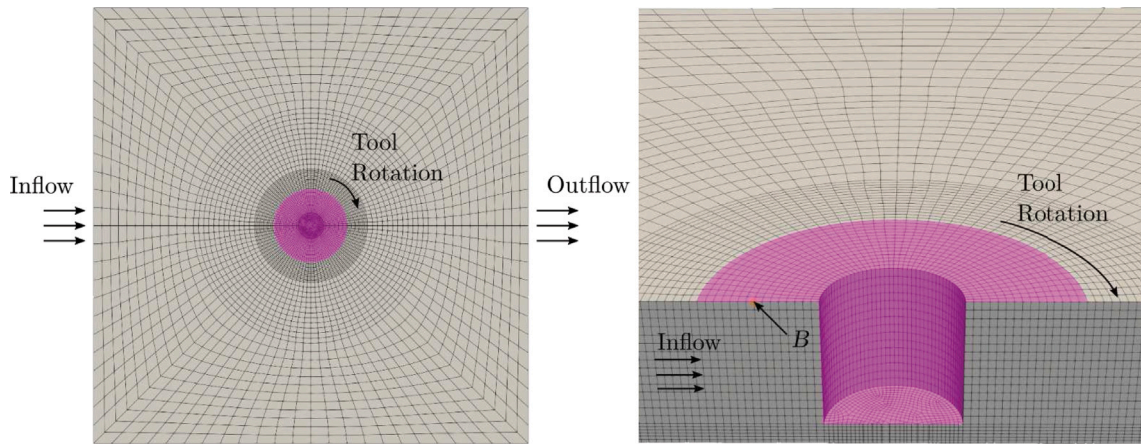
Fig. 18. Mesh of the three-dimensional FSW case which highlighted tool contact area.
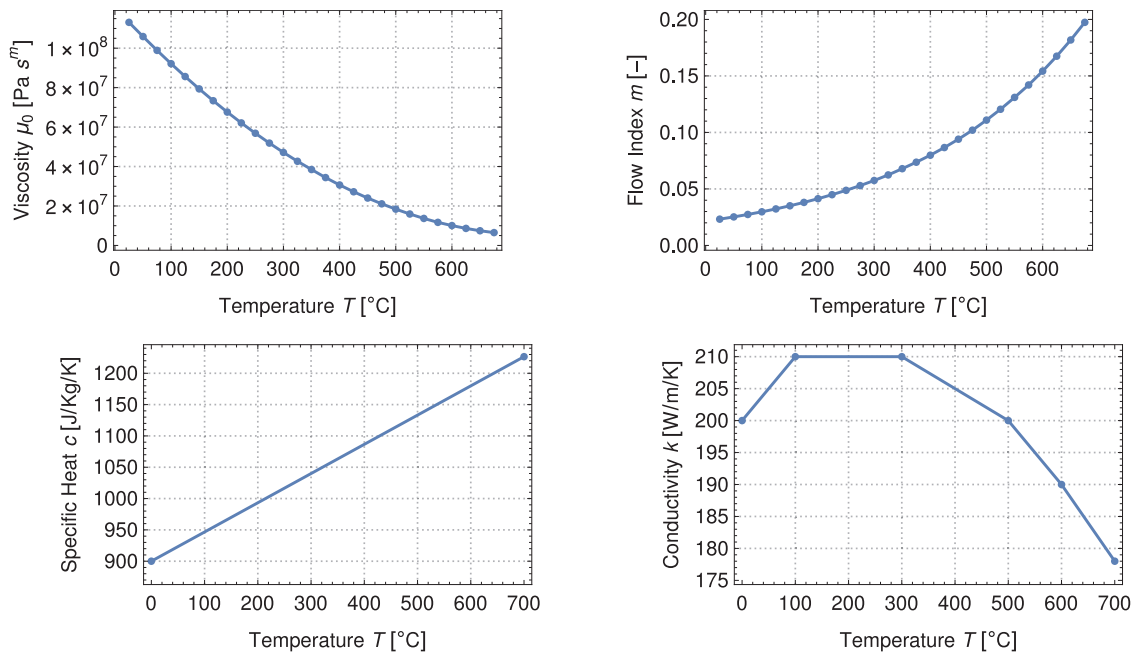

Fig. 19. Temperature dependency of mechanical and thermal material parameters.

5.4.2. Loading and boundary conditions

The FSW process is simulated assuming a pin-tool rotation with an angular velocity of $f_{tool} = 100$ RPM. This rotation induces a maximum linear velocity on the outermost points of the shoulder of $u_{max} = 0.094248$ m/s. The pin-tool longitudinal movement (welding speed) is prescribed as a Dirichlet boundary condition for the sheet (relative movement). Therefore, at the front surface (labeled as *Inflow*) a constant inflow speed is prescribed at $u_{in} = 0.008333$ m/s. At the back surface (labeled *Outflow*) no Dirichlet boundary conditions are applied, allowing for the material to exit the domain. The material flow is assumed to be isochoric and slip wall boundary conditions are assumed for the rest of the surfaces defining the computational domain.

The interaction between the FSW pin-tool (not modeled) and the sheet is accounted for by prescribing its angular velocity at the (highlighted) contact surface. For the sake of simplicity, the friction law has been replaced by a fully-stick condition (Dirichlet condition). A study of different friction laws, to better capture the interaction between the pin-tool and the sheet can be found in [8].

The initial temperature as well as the environment temperature is set to 25 ° C. The heat conduction flow is set through the bottom surface into the back plate. The heat transfer coefficient by conduction is set to $h_{cond} = 2500$ W/m^2/K.
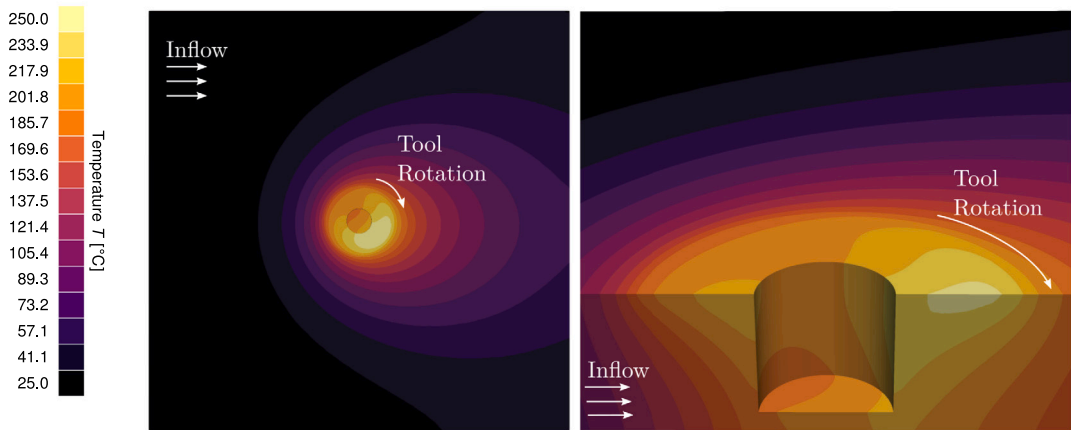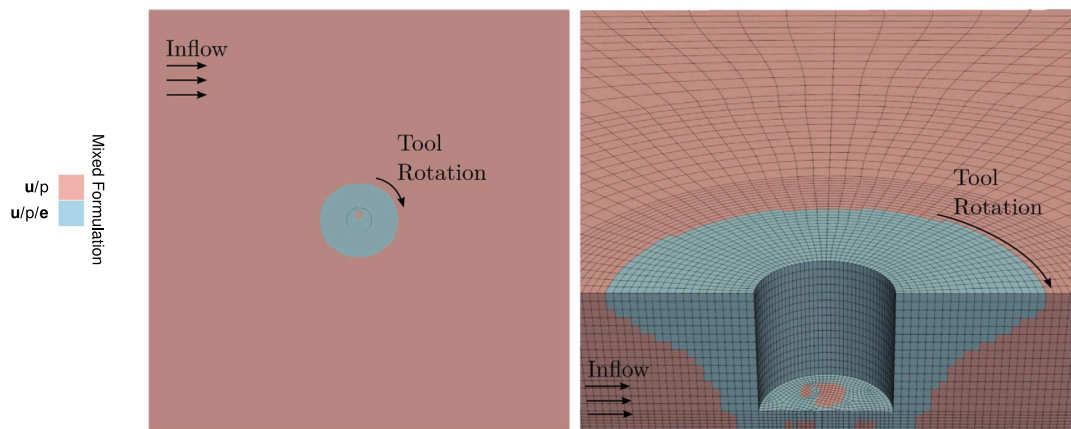
(a) velocity magnitude

(b) Streamlines

(c) Pressure
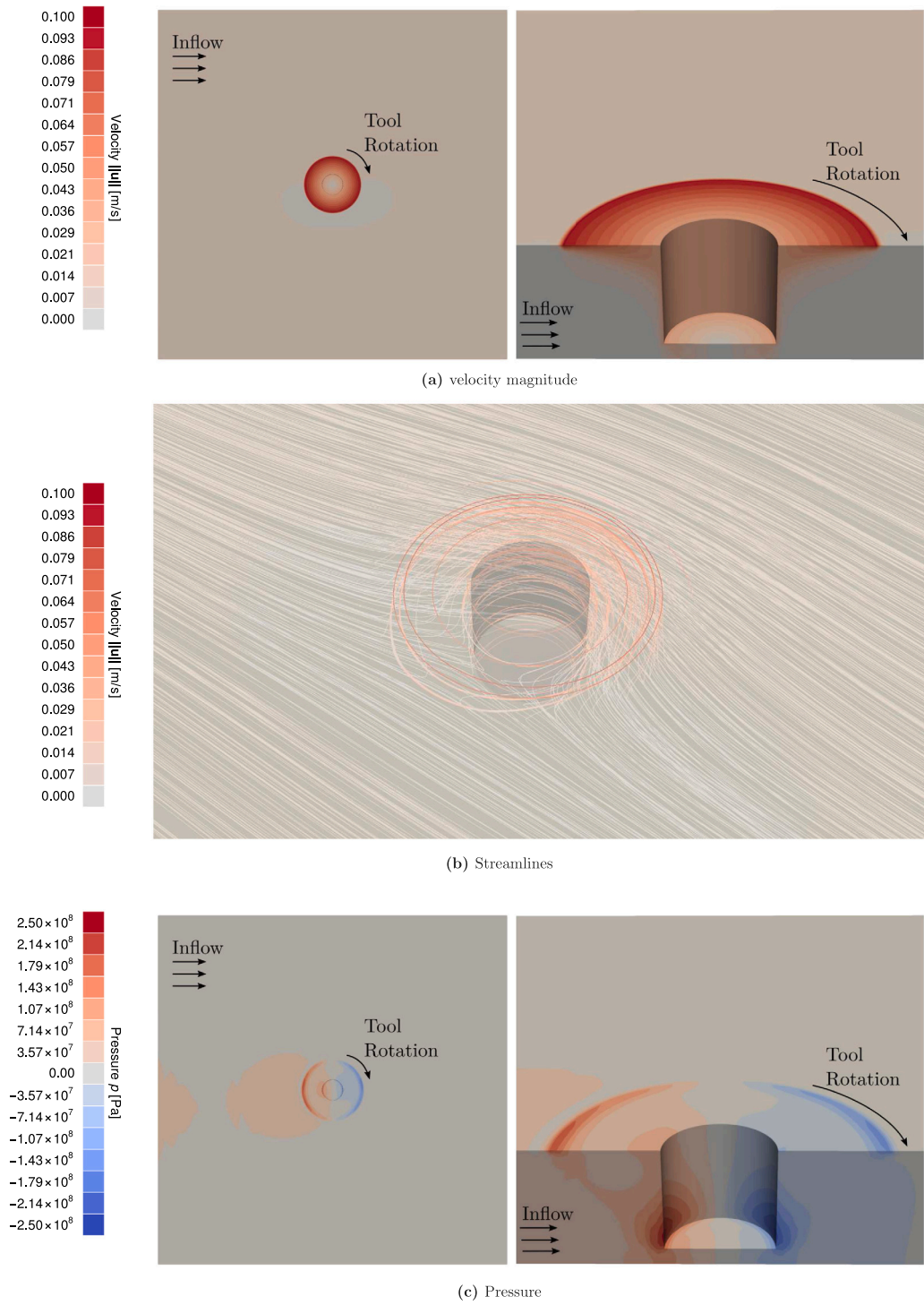
Fig. 20. Contour plots of various fields at $t_{30} = 0.15$ s.
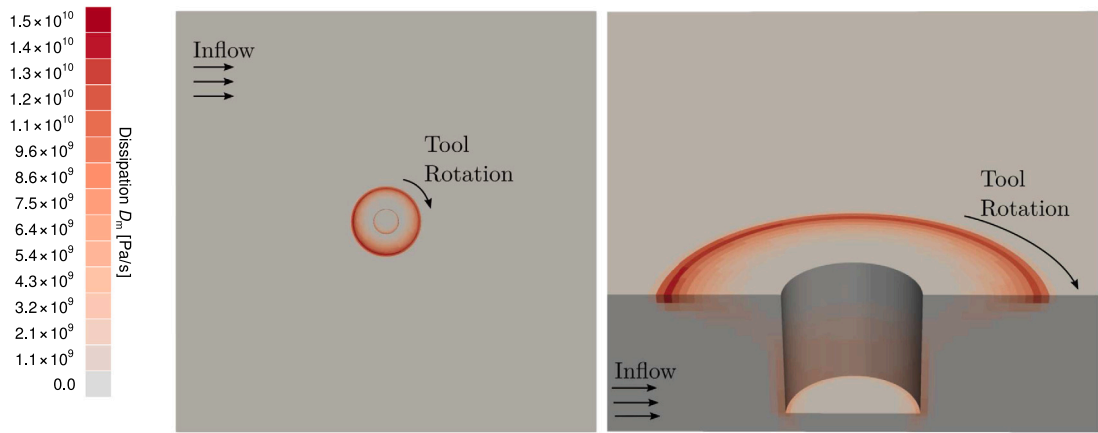
(d) Dissipation

(e) Temperature

(f) $\mathbf{u}/p$ and $\mathbf{u}/p/\mathbf{e}$ subdomains

Fig. 20. (*continued*).

(a) Temperature

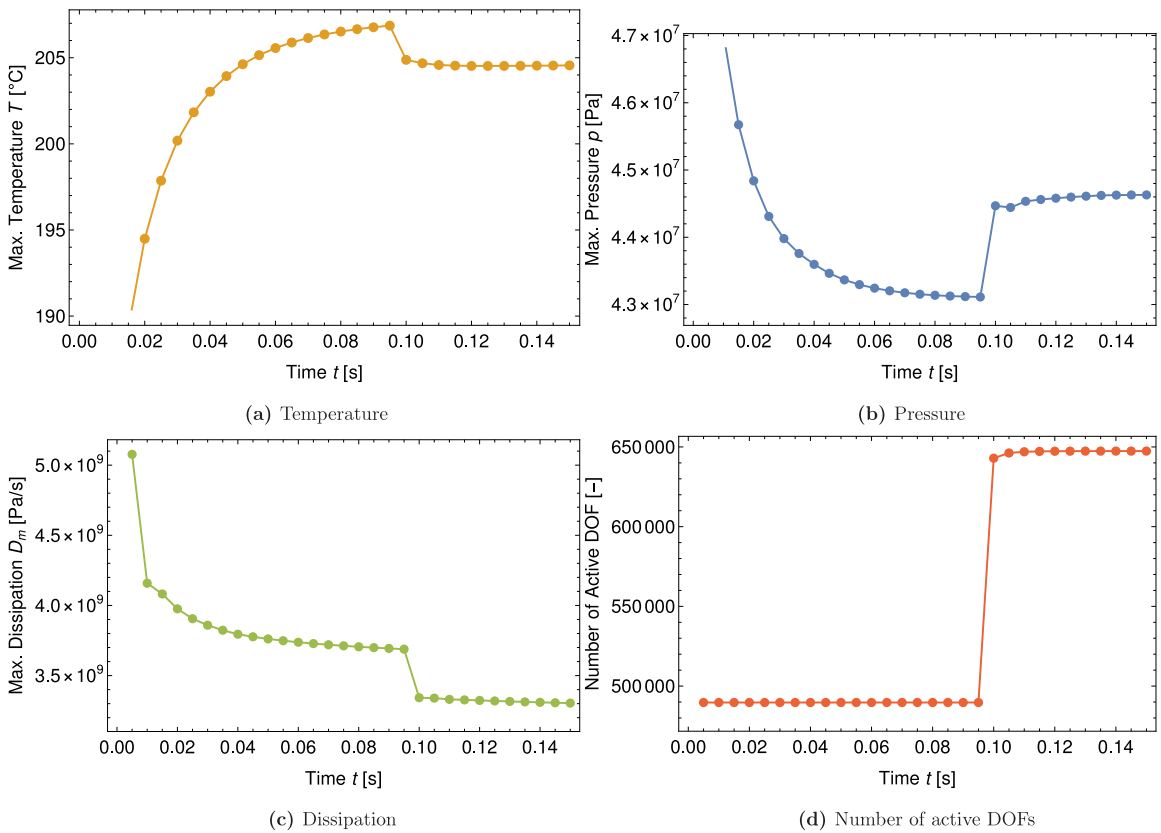(b) Pressure

(c) Dissipation

(d) Number of active DOFs

Fig. 21. Change of variables over time at point *B*.

All boundary conditions are applied at the beginning of the simulation (first time step) and are held constant throughout the entire simulation. In total, 30 time steps ($t_0 = 0$ s to $t_{30} = 0.15$ s) are computed. During the first 20 steps, the refinement criteria is disabled, allowing only for $\mathbf{u}/p$ elements to be used. Therefore, the steady state temperature field is reached as quickly as possible. At time step 20 ($t_{20} = 0.10$ s), the refinement criteria (based on a Zienkiewicz–Zhu (ZZ) error estimator with an error threshold of $1 \cdot 10^{-13}$) is enabled and all elements which exceed the specified error threshold become $\mathbf{u}/p/\mathbf{e}$ elements. After the activation of the $\mathbf{u}/p/\mathbf{e}$ elements, a new and more accurate steady state solution is reached.

5.4.3. Material law parameters

As introduced in Section 2.2, most material parameters are temperature-dependent as shown in Fig. 19. The fraction of the mechanical dissipation that is turned into heat (see Eq. (6)), is set to $\varphi = 0.8$. The density of the material is set to $\rho_0 = 2700$ kg/m^3 and the artificial speed-up parameter (see Eq. (27)) to faster reach the steady state is set to $\alpha = 100$.

5.4.4. Results

The presentation and discussion of the results is split into two parts. First, the different solution fields at the last time step ($t_{30} = 0.15$ s) are shown as contour plots in Fig. 20. This allows to assess the results as a solution of the FSW analysis. Second, selected variables at a fixed point in the computational domain are plotted over time to show their sensitivity towards changing from $\mathbf{u}/p$ to $\mathbf{u}/p/\mathbf{e}$ in parts of the domain.

The velocity field (Fig. 20a) is dominated by the Dirichlet boundary condition. The *shear-thinning* behavior of the applied material model can be clearly seen. Due to the high strain rates at the boundary layer, the viscosity decreases, causing a thinner boundary layer. Consequently, very high velocity gradients can be observed perpendicular to the top surface, further enhancing the shear-thinning effect. The same effect can be observed in Fig. 20b: only the streamlines closest to the pin and the shoulder are influenced by the tools rotation, whereas most other streamlines are relatively straight.

The pressure distribution (Fig. 20c) is almost symmetric and shows a spike on both the positive and the negative side where the shoulder of the tool ends. This is the expected result for the given boundary conditions. Using a proper friction model would yield more realistic results.

As expected, the contour plot of the dissipation (Fig. 20d) shows its highest values under the outermost part of the shoulder. Due to the shear-thinning behavior of the material model, the dissipation quickly drops by orders of magnitudes at a small distance to the tool-workpiece interface.

The temperature distribution (Fig. 20e) in the far-field shows a symmetric shape, while under the shoulder of the tool, the influence of the tools rotation can be seen. Furthermore, the influence of the convective term can be clearly seen.

The final plot (Fig. 20f) shows the $\mathbf{u}/p$ and $\mathbf{u}/p/\mathbf{e}$ subdomains. The area covered by $\mathbf{u}/p/\mathbf{e}$ elements is slightly larger than the area with significant dissipation, indicating that the refinement criterion and error threshold were well chosen.

Finally, Fig. 21 shows the evolution of different variables over time. The evolution of the temperature, pressure and dissipation (Figs. 21(a) to 21(c)) refers to point *B* (see Fig. 18). The fourth plot (Fig. 21(d)) is the number of active DOFs of the problem. In the first 20 steps ($t_0 = 0$ s to $t_{20} = 0.1$ s) only $\mathbf{u}/p$ elements are used. After activating the refinement criteria, the number of active DOFs increases by about 30%. The activation of the $\mathbf{u}/p/\mathbf{e}$ elements quickly leads to a new steady state.

It can be clearly seen from the plots, how temperature, pressure and dissipation change significantly after the activation of the $\mathbf{u}/p/\mathbf{e}$ elements—despite the already very fine mesh. As expected, the largest change can be observed for the dissipation, since the dissipation depends on both the strains and stresses. Thus, by employing the $\mathbf{u}/p/\mathbf{e}$ formulation, both fields are much more accurate.

Note that the new steady state is reached within 3 time steps. This emphasizes another advantage of the AFR method. It is possible to use the computationally cheaper $\mathbf{u}/p$ formulation to reach the steady state as quickly as possible and enhance the solution quality by locally activating the $\mathbf{u}/p/\mathbf{e}$ formulation.

6. Conclusions

In this paper, the proposed Adaptive Formulation Refinement method is used to define a computationally efficient framework for Friction Stir Welding simulations. The three-field $\mathbf{u}/p/\mathbf{e}$ formulation is used to enhance the strain and dissipation accuracy close the pin-tool, while the two-field $\mathbf{u}/p$ formulation is adopted to reduce the computational cost elsewhere. The use of linear Finite Elements is preserved for all unknowns by using a stabilized approach, the incompressible flow of the material is captured correctly and any remeshing is avoided. The AFR method is driven by the Zienkiewicz–Zhu a posteriori error estimator and the treatment of the interface between refined and unrefined subdomains is straightforward, due to the consistency of the variable fields and the lack of hanging nodes.

The global convergence study shows that the accuracy of the AFR method compares favorably to the $\mathbf{u}/p/\mathbf{e}$ formulation, while solving a system of equations with fewer active DOFs, thus resulting in faster build and solve times.

Finally, the developed method is applied to an FSW problem. First, the steady state of the problem is reached with a small computational cost by using the two-field formulation. Thereafter, the solution quality is enhanced in the highly dissipative area around the tool-sheet-interface, by switching to the three-field formulation according to the error estimator. Therefore the precision is very similar to the one of the three-field formulation but at a much lower computational cost.

Declaration of competing interest

The authors declare that they have no known competing financial interests or personal relationships that could have appeared to influence the work reported in this paper.

Data availability

Data will be made available on request.

References

[1] M. Chiumenti, et al., Numerical modeling of friction stir welding processes, Comput. Methods Appl. Mech. Engrg. 254 (2013) 353–369, http://dx.doi.org/10.1016/j.cma.2012.09.013.

[2] N. Dialami, et al., Challenges in thermo-mechanical analysis of friction stir welding processes, Arch. Comput. Methods Eng. 24 (1) (2016) 189–225, http://dx.doi.org/10.1007/s11831-015-9163-y.

[3] R. Padmanaban, V. Ratna Kishore, V. Balusamy, Numerical simulation of temperature distribution and material flow during friction stir welding of dissimilar aluminum alloys, Procedia Eng. 97 (2014) 854–863, http://dx.doi.org/10.1016/j.proeng.2014.12.360.

[4] Saad B. Aziz, et al., Impact of friction stir welding (FSW) process parameters on thermal modeling and heat generation of aluminum alloy joints, Acta Metall. Sin. (English Letters) 29 (9) (2016) 869–883, http://dx.doi.org/10.1007/s40195-016-0466-2.

[5] Rahul Kumar, V. Pancholi, R.P. Bharti, Material flow visualization and determination of strain rate during friction stir welding, J. Mater Process. Technol. 255 (2018) 470–476, http://dx.doi.org/10.1016/j.jmatprotec.2017.12.034.

[6] Narges Dialami, Miguel Cervera, Michele Chiumenti, Defect formation and material flow in friction stir welding, Eur. J. Mech. A Solids 80 (2020) 103912, http://dx.doi.org/10.1016/j.euromechsol.2019.103912.

[7] C. Leitão, et al., Material flow in friction stir welding, Microsc. Microanal. 14 (S3) (2008) 87–90, http://dx.doi.org/10.1017/s1431927608089472.

[8] N. Dialami, et al., Enhanced friction model for friction stir welding (FSW) analysis: Simulation and experimental validation, Int. J. Mech. Sci. 133 (2017) 555–567, http://dx.doi.org/10.1016/j.ijmecsci.2017.09.022.

[9] D.G. Andrade, et al., Analysis of contact conditions and its influence on strain rate and temperature in friction stir welding, Int. J. Mech. Sci. 191 (2021) 106095, http://dx.doi.org/10.1016/j.ijmecsci.2020.106095.

[10] Philippe Bussetta, et al., Comparison of a fluid and a solid approach for the numerical simulation of friction stir welding with a non-cylindrical pin, Steel Res. Int. 85 (6) (2013) 968–979, http://dx.doi.org/10.1002/srin.201300182.

[11] Narges Dialami, Miguel Cervera, Michele Chiumenti, Numerical modelling of microstructure evolution in friction stir welding (FSW), Metals 8 (3) (2018) http://dx.doi.org/10.3390/met8030183, URL: https://www.mdpi.com/2075-4701/8/3/183.

[12] M. Chiumenti, et al., Stress, strain and dissipation accurate 3-field formulation for inelastic isochoric deformation, Finite Elem. Anal. Des. 192 (2021) 103534, http://dx.doi.org/10.1016/j.finel.2021.103534.

[13] T.J.R. Hughes, Equivalence of finite elements for nearly incompressible elasticity, J. Appl. Mech. 44 (1) (1977) 181–183, http://dx.doi.org/10.1115/1.3423994.

[14] David S. Malkus, Thomas J.R. Hughes, Mixed finite element methods — Reduced and selective integration techniques: A unification of concepts, Comput. Methods Appl. Mech. Engrg. 15 (1) (1978) 63–81, http://dx.doi.org/10.1016/0045-7825(78)90005-1.

[15] Thomas J.R. Hughes, Generalization of selective integration procedures to anisotropic and nonlinear media, Internat. J. Numer. Methods Engrg. 15 (9) (1980) 1413–1418, http://dx.doi.org/10.1002/nme.1620150914.

[16] E.A. Souza de Neto, et al., Design of simple low order finite elements for large strain analysis of nearly incompressible solids, Int. J. Solids Struct. 33 (20–22) (1996) 3277–3296, http://dx.doi.org/10.1016/0020-7683(95)00259-6.

[17] L. De Vivo, F. Marotti de Sciarra, The B-bar method and the limitation principles, Int. J. Solids Struct. 36 (34) (1999) 5177–5206, http://dx.doi.org/10.1016/s0020-7683(98)00233-9.

[18] E.A. de Souza Neto, F.M. Andrade Pires, D.R.J. Owen, F-bar-based linear triangles and tetrahedra for finite strain analysis of nearly incompressible solids. Part I: formulation and benchmarking, Internat. J. Numer. Methods Engrg. 62 (3) (2005) 353–383, http://dx.doi.org/10.1002/nme.1187.

[19] Y. Onishi, R. Iida, K. Amaya, F-bar aided edge-based smoothed finite element method using tetrahedral elements for finite deformation analysisof nearly incompressible solids, Internat. J. Numer. Methods Engrg. 109 (11) (2016) 1582–1606, http://dx.doi.org/10.1002/nme.5337.

[20] J.C. Simo, M.S. Rifai, A class of mixed assumed strain methods and the method of incompatible modes, Internat. J. Numer. Methods Engrg. 29 (8) (1990) 1595–1638, http://dx.doi.org/10.1002/nme.1620290802.

[21] E.A. Souza de Neto, et al., Remarks on the stability of enhanced strain elements in finite elasticity and elastoplasticity, Commun. Numer. Methods. Eng. 11 (11) (1995) 951–961, http://dx.doi.org/10.1002/cnm.1640111109.

[22] Andreas Krischok, Christian Linder, On the enhancement of low-order mixed finite element methods for the large deformation analysis of diffusion in solids, Internat. J. Numer. Methods Engrg. 106 (4) (2015) 278–297, http://dx.doi.org/10.1002/nme.5120.

[23] J.C. Simo, R.L. Taylor, K.S. Pister, Variational and projection methods for the volume constraint in finite deformation elasto-plasticity, Comput. Methods Appl. Mech. Engrg. 51 (1–3) (1985) 177–208, http://dx.doi.org/10.1016/0045-7825(85)90033-7.

[24] Peter Hansbo, Mats G. Larson, Discontinuous Galerkin methods for incompressible and nearly incompressible elasticity by Nitsche's method, Comput. Methods Appl. Mech. Engrg. 191 (17–18) (2002) 1895–1908, http://dx.doi.org/10.1016/s0045-7825(01)00358-9.

[25] Bernardo Cockburn, Dominik Schötzau, Jing Wang, Discontinuous Galerkin methods for incompressible elastic materials, Comput. Methods Appl. Mech. Engrg. 195 (25–28) (2006) 3184–3204, http://dx.doi.org/10.1016/j.cma.2005.07.003.

[26] Adrian Lew, Alex Ten Eyck, Ramsharan Rangarajan, Some applications of discontinuous Galerkin methods in solid mechanics, in: IUTAM Symposium on Theoretical, Computational and Modelling Aspects of Inelastic Media, Springer Netherlands, 2008, pp. 227–236, http://dx.doi.org/10.1007/978-1-4020-9090-5_21.

[27] Thomas J.R. Hughes, Multiscale phenomena: Green's functions, the Dirichlet-to-Neumann formulation, subgrid scale models, bubbles and the origins of stabilized methods, Comput. Methods Appl. Mech. Engrg. 127 (1–4) (1995) 387–401, http://dx.doi.org/10.1016/0045-7825(95)00844-9.

[28] Thomas J.R. Hughes, et al., The variational multiscale method—a paradigm for computational mechanics, Comput. Methods Appl. Mech. Engrg. 166 (1–2) (1998) 3–24, http://dx.doi.org/10.1016/s0045-7825(98)00079-6.

[29] M. Chiumenti, et al., A stabilized formulation for incompressible elasticity using linear displacement and pressure interpolations, Comput. Methods Appl. Mech. Engrg. 191 (46) (2002) 5253–5264, http://dx.doi.org/10.1016/s0045-7825(02)00443-7.

[30] Antoinette M. Maniatty, et al., Stabilized finite element method for viscoplastic flow: formulation and a simple progressive solution strategy, Comput. Methods Appl. Mech. Engrg. 190 (35–36) (2001) 4609–4625, http://dx.doi.org/10.1016/s0045-7825(00)00346-7.

[31] Antoinette M. Maniatty, Yong Liu, Stabilized finite element method for viscoplastic flow: formulation with state variable evolution, Internat. J. Numer. Methods Engrg. 56 (2) (2002) 185–209, http://dx.doi.org/10.1002/nme.554.

[32] M. Cervera, et al., Mixed linear/linear simplicial elements for incompressible elasticity and plasticity, Comput. Methods Appl. Mech. Engrg. 192 (49–50) (2003) 5249–5263, http://dx.doi.org/10.1016/j.cma.2003.07.007.

[33] M. Cervera, et al., Softening, localization and stabilization: capture of discontinuous solutions in J2 plasticity, Int. J. Numer. Anal. Methods Geomech. 28 (5) (2004) 373–393, http://dx.doi.org/10.1002/nag.341.

[34] M. Cervera, M. Chiumenti, C. Agelet de Saracibar, Shear band localization via local J2 continuum damage mechanics, Comput. Methods Appl. Mech. Engrg. 193 (9–11) (2004) 849–880, http://dx.doi.org/10.1016/j.cma.2003.11.009.

[35] C. Agelet de Saracibar, et al., On the orthogonal subgrid scale pressure stabilization of finite deformation J2 plasticity, Comput. Methods Appl. Mech. Engrg. 195 (9–12) (2006) 1224–1251, http://dx.doi.org/10.1016/j.cma.2005.04.007.

[36] Antoinette M. Maniatty, et al., Higher order stabilized finite element method for hyperelastic finite deformation, Comput. Methods Appl. Mech. Engrg. 191 (13–14) (2002) 1491–1503, http://dx.doi.org/10.1016/s0045-7825(01)00335-8.

[37] Arif Masud, Timothy J. Truster, A framework for residual-based stabilization of incompressible finite elasticity: Stabilized formulations and $\bar{F}$ methods for linear triangles and tetrahedra, Comput. Methods Appl. Mech. Engrg. 267 (2013) 359–399, http://dx.doi.org/10.1016/j.cma.2013.08.010.

[38] Guglielmo Scovazzi, et al., A simple, stable, and accurate linear tetrahedral finite element for transient, nearly, and fully incompressible solid dynamics: a dynamic variational multiscale approach, Internat. J. Numer. Methods Engrg. 106 (10) (2015) 799–839, http://dx.doi.org/10.1002/nme.5138.

[39] S. Rossi, N. Abboud, G. Scovazzi, Implicit finite incompressible elastodynamics with linear finite elements: A stabilized method in rate form, Comput. Methods Appl. Mech. Engrg. 311 (2016) 208–249, http://dx.doi.org/10.1016/j.cma.2016.07.015.

[40] Xianyi Zeng, et al., A dynamic variational multiscale method for viscoelasticity using linear tetrahedral elements, Internat. J. Numer. Methods Engrg. 112 (13) (2017) 1951–2003, http://dx.doi.org/10.1002/nme.5591.

[41] Inocencio Castañar, Joan Baiges, Ramon Codina, A stabilized mixed finite element approximation for incompressible finite strain solid dynamics using a total Lagrangian formulation, Comput. Methods Appl. Mech. Engrg. 368 (2020) 113164, http://dx.doi.org/10.1016/j.cma.2020.113164.

[42] H. Nguyen, p-Adaptive and Automatic Hp-Adaptive Finite Element Methods for Elliptic Partial Differential Equations (Ph.D. thesis), UC San Diego, 2010, URL: https://escholarship.org/uc/item/8cv6d65z.

[43] Robert D. Russell, Adaptive mesh refinement, in: Encyclopedia of Applied and Computational Mathematics, Springer Berlin Heidelberg, 2015, pp. 23–25, http://dx.doi.org/10.1007/978-3-540-70529-1_341.

[44] M. Cervera, M. Chiumenti, R. Codina, Mixed stabilized finite element methods in nonlinear solid mechanics. part I: Formulation, Comput. Methods Appl. Mech. Engrg. 199 (37–40) (2010) 2559–2570, http://dx.doi.org/10.1016/j.cma.2010.04.006.

[45] G. Scovazzi, T. Song, X. Zeng, A velocity/stress mixed stabilized nodal finite element for elastodynamics: Analysis and computations with strongly and weakly enforced boundary conditions, Comput. Methods Appl. Mech. Engrg. 325 (2017) 532–576, http://dx.doi.org/10.1016/j.cma.2017.07.018.

[46] M. Chiumenti, M. Cervera, R. Codina, A mixed three-field FE formulation for stress accurate analysis including the incompressible limit, Comput. Methods Appl. Mech. Engrg. 283 (2015) 1095–1116, http://dx.doi.org/10.1016/j.cma.2014.08.004.

[47] M. Cervera, M. Chiumenti, R. Codina, Mixed stabilized finite element methods in nonlinear solid mechanics. part II: Strain localization, Comput. Methods Appl. Mech. Engrg. 199 (37–40) (2010) 2571–2589, http://dx.doi.org/10.1016/j.cma.2010.04.005.

[48] M. Cervera, et al., Mixed stabilized finite element methods in nonlinear solid mechanics. part III: Compressible and incompressible plasticity, Comput. Methods Appl. Mech. Engrg. 285 (2015) 752–775, http://dx.doi.org/10.1016/j.cma.2014.11.040.

[49] Carlos A. Moreira, et al., Accurate thermal-induced structural failure analysis under incompressible conditions, Eng. Struct. 261 (2022) 114213, http://dx.doi.org/10.1016/j.engstruct.2022.114213.

[50] Inocencio Castañar, et al., Topological derivative-based topology optimization of incompressible structures using mixed formulations, Comput. Methods Appl. Mech. Engrg. 390 (2022) 114438, http://dx.doi.org/10.1016/j.cma.2021.114438.

[51] Mark Ainsworth, J.Tinsley Oden, A posteriori error estimation in finite element analysis, Comput. Methods Appl. Mech. Engrg. 142 (1–2) (1997) 1–88, http://dx.doi.org/10.1016/s0045-7825(96)01107-3.

[52] O.C. Zienkiewicz, J.Z. Zhu, A simple error estimator and adaptive procedure for practical engineerng analysis, Internat. J. Numer. Methods Engrg. 24 (2) (1987) 337–357, http://dx.doi.org/10.1002/nme.1620240206.

[53] R. Verfürth, A review of a posteriori error estimation techniques for elasticity problems, Comput. Methods Appl. Mech. Engrg. 176 (1–4) (1999) 419–440, http://dx.doi.org/10.1016/s0045-7825(98)00347-8.

[54] Rüdiger Verfürth, A Posteriori Error Estimation Techniques for Finite Element Methods, Oxford University Press, 2013, http://dx.doi.org/10.1093/acprof:oso/9780199679423.001.0001.

[55] T. Sheppard, D.S. Wright, Determination of flow stress: Part 1 constitutive equation for aluminium alloys at elevated temperatures, Met. Technol. 6 (1) (1979) 215–223, http://dx.doi.org/10.1179/030716979803276264.

[56] Daniel Dall'Onder dos Santos, et al., Numerical approximations for flow of viscoplastic fluids in a lid-driven cavity, J. Non-Newton. Fluid Mech. 166 (12–13) (2011) 667–679, http://dx.doi.org/10.1016/j.jnnfm.2011.03.004.

[57] Pierre J. Carreau, Rheological equations from molecular network theories, Trans. Soc. Rheol. 16 (1) (1972) 99–127, http://dx.doi.org/10.1122/1.549276.

[58] F.H. Norton, The Creep of Steel At High Temperatures, in: Bulletin, McGraw-Hill book Company, Incorporated, 1929, URL: https://books.google.de/books?id=vswxAAAAMAAJ.

[59] Nicholas John Hoff, Approximate analysis of structures in the presence of moderately large creep deformations, Quart. Appl. Math. 12 (1954) 49–55.

[60] Franco Brezzi, Michel Fortin (Eds.), Mixed and hybrid finite element methods, Springer New York, 1991, http://dx.doi.org/10.1007/978-1-4612-3172-1.

[61] Ramon Codina, Stabilization of incompressibility and convection through orthogonal sub-scales in finite element methods, Comput. Methods Appl. Mech. Engrg. 190 (13–14) (2000) 1579–1599, http://dx.doi.org/10.1016/s0045-7825(00)00254-1.

[62] Ramon Codina, Jordi Blasco, Stabilized finite element method for the transient Navier–Stokes equations based on a pressure gradient projection, Comput. Methods Appl. Mech. Engrg. 182 (3–4) (2000) 277–300, http://dx.doi.org/10.1016/s0045-7825(99)00194-2.

[63] Ramon Codina, Stabilized finite element approximation of transient incompressible flows using orthogonal subscales, Comput. Methods Appl. Mech. Engrg. 191 (39–40) (2002) 4295–4321, http://dx.doi.org/10.1016/s0045-7825(02)00337-7.

[64] N. Dialami, et al., A fast and accurate two-stage strategy to evaluate the effect of the pin tool profile on metal flow, torque and forces in friction stir welding, Int. J. Mech. Sci. 122 (2017) 215–227, http://dx.doi.org/10.1016/j.ijmecsci.2016.12.016.

[65] C. Agelet de Saracibar, et al., Computational modeling and sub-grid scale stabilization of incompressibility and convection in the numerical simulation of friction stir welding processes, Arch. Comput. Methods Eng. 21 (1) (2014) 3–37, http://dx.doi.org/10.1007/s11831-014-9094-z.

[66] Satish Balay, et al., PETSc/TAO Users Manual, Tech Report ANL-21/39 - Revision 3.16, Argonne National Laboratory, 2021.

[67] J.E. Akin, An introduction to the fem and adaptive error analysis for engineering students, in: Finite Element Analysis with Error Estimators, Elsevier, 2005, http://dx.doi.org/10.1016/b978-0-7506-6722-7.x5030-9.